J. Fluid Mech. (2005), *vol.* 539, *pp.* 349–385.
doi:10.1017/S002211200500546X Printed in the United Kingdom

On gravity currents driven by constant fluxes of saline and particle-laden fluid in the presence of a uniform flow

By ANDREW J. HOGG[1], MARK A. HALLWORTH[2] AND HERBERT E. HUPPERT[2]

[1]Centre for Environmental and Geophysical Flows, School of Mathematics, University of Bristol, University of Bristol, Bristol BS8 1TW, UK
a.j.hogg@bris.ac.uk

[2]Institute of Theoretical Geophysics, Department of Applied Mathematics & Theoretical Physics, University of Cambridge, Wilberforce Rd, Cambridge CB4 0WA, UK
hallwort@esc.cam.ac.uk, heh1@esc.cam.ac.uk

(Received 13 September 2004 and in revised form 29 March 2005)

Experiments are reported on the sustained release of saline and particle-laden fluid into a long, but relatively narrow, flume, filled with fresh water. The dense fluid rapidly spread across the flume and flowed away from the source: the motion was then essentially two-dimensional. In the absence of a background flow in the flume, the motion was symmetric, away from the source. However, in the presence of a background flow the upstream speed of propagation was slowed and the downstream speed was increased. Measurements of this motion are reported and, when the excess density was due to the presence of suspended sediment, the distribution of the deposited particles was also determined. Alongside this experimental programme, new theoretical models of the motion were developed. These were based upon multi-layered depth-averaged shallow-water equations, in which the interfacial drag and mixing processes were explicitly modelled. While the early stages of the motion are independent of these interfacial phenomena to leading order, they play an increasingly important dynamical role as the the flow is slowed, or even arrested. In addition a new integral model is proposed. This does not resolve the interior dynamics of the flow, but may be readily integrated and obviates the need for more lengthy numerical calculations. It is shown that the predictions from both the shallow-layer and integral models are in close agreement with the experimental observations.

1. Introduction

Owing to their wide application to physical systems as diverse as coastal sea breezes, sediment-transporting currents in the deep ocean, volcanic ash clouds and estuarine flows, gravity currents and their dynamics have been extensively researched during recent years. In essence all of these phenomena are driven by the gravitational force associated with the density difference between the intruding and surrounding fluid, which leads to the flow of the denser fluid under the less dense and along the underlying boundary. In this study we investigate experimentally and theoretically the motion of gravity currents, driven by sustained sources of saline or particle-laden fluid, through an ambient fluid, which is independently flowing.

The interaction between ambient flow and density-driven motion has many applications. For example within estuaries, oceanic saline water may be arrested by a fresh riverine flow to form a salt wedge (Schijf & Schönfeld 1953). Alternatively relatively dense particulate pollutants may be discharged within a river or coastal region and their dispersion is controlled by the competition between the density-induced motion and the environmental currents (Hogg & Huppert 2001). Similarly, the dispersion of dense, toxic gas within the atmosphere arises through a combination of density-driven spreading and transport by the wind (Rottman, Hunt & Mercer 1985). Finally, atmospheric cool pools, which are formed by the downdraught of cold air and which may trigger large-scale convection, spread due to their excess density relative to the surrounding air and are advected by the background wind, thus altering the rate with which they are heated (Ross, Tompkins & Parker 2004).

The fundamental dynamics of sustained, relatively dense flow with co- or anti-flowing ambient fluids have been studied experimentally before. Notably Simpson & Britter (1980) introduced saline fluid into a co-moving ambient and arrest the advance of the dense fluid by the use of a moving belt. They deduced empirically that the speed of the gravity current was a linear combination of the gravity-driven motion and a constant fraction of the mean flow. In their experimental regime they found that the motion of the gravity current is by increased a fraction 0.62 of the mean flow. Bühler, Wright & Kim (1991) studied this type of motion using a different experimental configuration. They injected saline and fresh fluids at one end of a long, narrow flume and measured the speed of the front of the dense fluid sufficiently downstream of the inlets so that the initial mixing processes were complete. Their data, which are approximately compatible with those of Simpson & Britter (1980), are compared with our results in § 4. This study builds upon these works and importantly we also consider the sustained flows of particle-laden suspensions. These differ from their saline counterparts because the density difference between the intruding suspension and the surrounding fluid is progressively diminished as the particles sediment out of the flow. In a previous contribution we studied instantaneous releases of dense suspensions in the presence of a background flow (Hallworth, Hogg & Huppert 1998); this paper extends our analysis to sustained sources. As will be demonstrated the different source conditions lead to considerable differences in the observed motion.

Theoretical formulations of varying complexity have been employed to model the motion of gravity currents. These include numerical simulations of the full equations of motion (Klemp, Rotunno & Skamarock 1994), depth-averaged models that exploit the shallowness of the flow (Rottman & Simpson 1983) and 'integral', or 'box', models that do not resolve the interior dynamics of the motion but capture the bulk characteristics (e.g. Huppert & Simpson 1980; Dade & Huppert 1995; Harris, Hogg & Huppert 2001). Our approach in this study is two-fold. We employ a multi-layered depth-averaged model that calculates the heights, densities and velocities of the mobile layer and the ambient fluid as functions of space and time. In addition we formulate a new, integral model for sustained flows that may be readily integrated to yield predictions that are very similar to the more complete model. Our approach throughout is one of simplicity; we formulate models that produce theoretical predictions in close agreement with the experimental measurements, but are relatively free of empirically determined parameters. Where we are forced to parameterize complex flow phenomena, such as the drag at the interface between co-moving fluids, we have chosen the very simplest parameterization, noting that more complex choices could be employed within the same analytical framework. However, as will be shown below, it does not seem necessary to facilitate the accurate prediction of our experimental observations.

As indicated above, there are close connections between the upstream flow of a gravity current and the arrested salt wedge structures found within estuaries. These occur provided the intensity of the turbulence and associated mixing processes are insufficient to mix the salty and fresh waters, leading to a stratified density profile with the dense saline fluid being over-ridden by the relatively fresh water (Lewis 1997). A leading-order model of these dynamical features assumes that the saline fluid is arrested and that the hydrostatic pressure gradient associated with the excess density is balanced by the interfacial drag between the stationary wedge and the fresh water flow (Schijf & Schönfeld 1953). Such a model provides a reasonable description of the motion, although the assumption that the lower layer of dense fluid is stationary is a significant simplification of the true flow. It has been observed that there is circulation within the dense layer and mixing between the two water masses, the intensity of which depends on the local velocity and density gradients (Lewis 1997). Arita & Jirka (1987*a*) address this weakness and formulate a model in which both of the layers flow and they parameterize the mixing and drag between the layers. This approach was later extended by Sorgard (1991) to form a three-layer model in which the fresh, salty and mixed layers were modelled separately. The long-term upstream motion of saline gravity currents shares many dynamical features with arrested salt wedges in that the effects of interfacial drag progressively slow the advance, alter the depth profile and eventually halt the progression. In these flows, there is a sustained source of dense fluid feeding the gravity current and so its motion may only be arrested if there is recirculation within the dense layer. We show how such a phenomenon may be captured within a layer-averaged model by developing the model proposed by Sorgard (1991) to permit the density of the mixed layer to evolve and crucially not to be assumed constant. We also formulate the first model of an arrested wedge when the excess density is due to the presence of suspended particles. We shall see that this gives the motion a rather different character.

This paper is organized as follows. First we describe our experimental procedure and the new observations of gravity currents driven by compositional differences between the intruding and ambient fluids or by suspended, relatively heavy particles, in the presence of a mean flow (§ 2). Here we emphasize the way in which these flows were generated and the differences between the upstream and downstream propagation. We then formulate a multi-layered shallow-water model of the flow (§ 3). This builds on previous models of particle-driven gravity currents (Bonnecaze, Huppert & Lister 1993) and of shallow salt wedges in estuaries (Schijf & Schönfeld 1953; Sorgard 1991). Comparisons between theory and experiments are given for saline flows in § 4 and for particle-laden flows in § 5. Additionally we discuss the long-time behaviour and illustrate the role of our new theoretical models. Finally we summarize our results in § 6 and draw some conclusions.

2. Experiments

2.1. *Experimental setup*

A series of experiments was performed to study the behaviour of buoyancy-driven motion arising from the input at a constant rate of dense fluid in the presence of a mean flow. The experimental apparatus was similar to the two-dimensional channel employed by Hallworth *et al.* (1998) modified to deliver a constant flux, rather than a fixed volume, of dense fluid into the ambient flow and is shown schematically in figure 1. The experiments were carried out in a Perspex channel of length 9.4 m, width 26 cm and height 50 cm. The channel was filled with water to a depth of 30 cm and a uniform

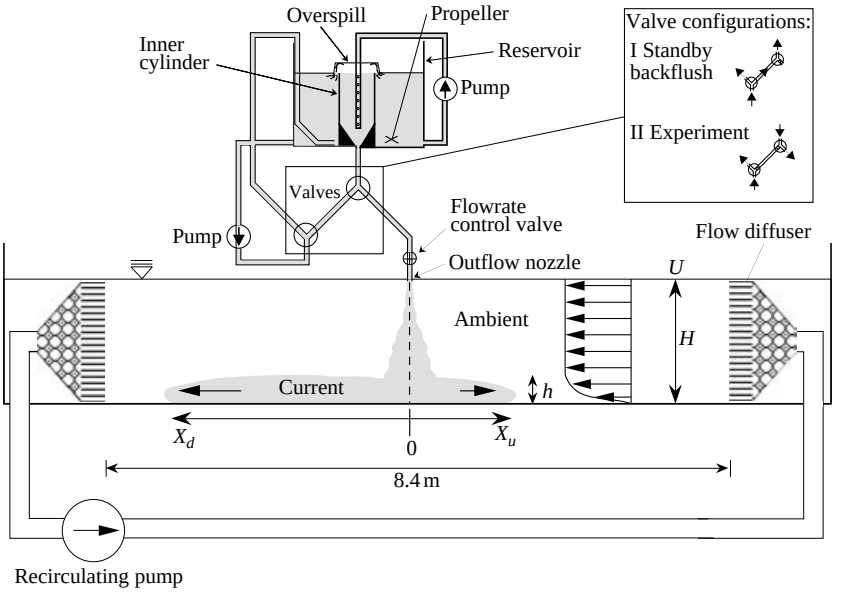

FIGURE 1. The experimental setup. The valve was used in two configurations I and II. Position I was used prior to initiating the flow to ensure that particles remained well-mixed throughout the inner cylinder. Position II was used during the experiment to provide additional mixing within the reservoir.

ambient flow established by pumping water at a fixed rate in a continuous loop via a hose connecting inlet and outlet ports at either end of the channel. As described in Hallworth *et al.* (1998), the velocity profile within the ambient flow was determined by use of a Sontek acoustic Doppler velocimeter. The velocity profiles measured at various distances upstream and downstream from the release point are shown in figure 4 of Hallworth *et al.* (1998). In summary, we found that the velocity was approximately uniform within the interior of the flow, with an average value of $3\,\mathrm{cm\,s^{-1}}$, although it decreased sharply within a basal boundary layer of approximate thickness 2 cm. There was a reduction in velocity towards the free surface. The Reynolds number of the flow, based upon the volume flux per unit width, was approximately 7000, well within the turbulent regime.

The focus of the series of experiments reported here was the evolution of buoyancy-driven flows resulting from the input of a constant flux of dense fluid. Since we wished to study the differences between upstream and downstream propagation, we introduced the dense fluid at the midpoint of the channel. The delivery was provided by a constant-head gravity feed from a 15 l reservoir, positioned approximately 50 cm above the free surface of the water in the channel. Rubber tubing connected the base of the reservoir via a valve to an 8 mm diameter metal nozzle, which was aligned vertically within the medial plane of the channel with its end just below the free surface of the water in the underlying channel. The flow rate could be adjusted by means of a variable control valve. On release from the reservoir, the dense fluid descended through the ambient and was deflected both upstream and downstream by the presence of the boundary, delivering approximately equal fluxes of fluid in each direction. The motion of the ambient fluid within the channel led to some deflection of the descending negatively buoyant jet, but this deflection was negligible in all but the lowest input fluxes. Of considerable importance, however, was the mixing with the ambient

fluid which occurred both during the descent and during the deflection by the underlying boundary. This mixing is discussed below (§ 2.4).

The dense fluids delivered into the channel were either saline solutions (§ 2.2) or well-mixed suspensions of silicon carbide particles (§ 2.3). For both of these we endeavoured to deliver the fluid at a constant rate and for the particle suspensions we also kept the reservoir well-mixed in order to maintain a constant concentration of particulate matter.

To maintain a constant input rate over a period of several minutes, the dense fluid was drained from the base of a constant-head inner cylinder installed within the reservoir, as depicted in figure 1. The cylinder was continually replenished by a pump drawing fluid from the base of the main body of the reservoir at a rate much faster than the nozzle outflow rate. The cylinder was thus continually overflowing into the main body of the reservoir, thereby sustaining a constant pressure head which implied a constant flux. The inner cylinder was of narrow bore (5.7 cm) and tapered towards the outlet to eliminate recirculation regions within which sediment could become trapped. The replenishment tube was aligned with the vertical axis of the cylinder and was punctured along its submerged length by small (1 mm) holes through which the dense fluid was pumped as high-velocity jets.

This arrangement permitted the delivery of fluid at a constant rate and avoided the loss of particles within the constant-head cylinder. However, to ensure that the fluid had a constant volume fraction of particles and to prevent sedimentation within the exit valve and tubing, two further procedures were implemented. First, a mechanical stirrer was installed to induce vigorous turbulence and fluid circulation within the reservoir and which maintained a well-mixed distribution of particles. Second, we installed an additional pump. It was first used to back-flush the inner cylinder and outlet valve prior to the start of each experiment (valve configuration I: figure 1). Thereafter it was switched to recirculating the main body of the reservoir (valve configuration II: figure 1), thus supplementing the fluid turbulence and the vertical mixing processes within the reservoir.

It should be emphasized that the design of the flow delivery system evolved to the configuration described above as a result of extensive tests which revealed that any less effort applied to the mixing of the suspension was insufficient to maintain a constant volume fraction of particles. These tests involved collecting a series of samples, delivered from the apparatus, over known periods of time, weighing the mass of the collected suspension and then decanting the excess fluid, and drying and weighing the particle content. We were thus able to assess the behaviour of the apparatus over periods of approximately 10 minutes. In the experiments reported below we employed volumetric flow rates in the range 25–100 $\mathrm{cm^3\,s^{-1}}$ and volumetric concentrations of particles in the range 0.8 %–3.2 %. We tested the device with a variety of particle sizes and found the concentration was approximately constant for silicon carbide particles with a mean diameter of 37 μm, or less. However the concentration of particles progressively reduced by approximately 15 % throughout the duration of the test when larger, 53 μm diameter, particles were used. This may be ascribed to there being a slight vertical distribution of concentration in the reservoir – and since fluid is withdrawn from the base of the reservoir, the concentration of particles delivered will progressively decrease. Elementary scaling suggests that the downward flux of particles scales as $v_s\phi$, where v_s the settling velocity of the particles and ϕ the volumetric concentration, while the upward flux, modelled by an eddy diffusivity scales as $a^2\omega\phi/h_r$, where h_r is the height of the reservoir, a the dimension of the mechanical stirrer and ω its rate of rotation. Thus the magnitude of the ratio $\Gamma = h_r v_s/a^2\omega$ will distinguish between

Experiment number	Volume flux Q ($\mathrm{cm^3\,s^{-1}}$)	Reduced gravity g' ($\mathrm{cm\,s^{-2}}$)	Duration D (s)	Ambient flow speed $\overline{u}$ ($\mathrm{cm\,s^{-1}}$)
1	51.7	64.5	120	2.9
2	51.7	64.5	120	2.9
3	51.7	121.1	105	2.9
4	51.7	33.5	150	2.9
5	51.5	33.5	165	0
6	51.7	17.1	150	2.9
7	51.8	17.1	172	0
8	51.6	121.1	105	0
9	52.1	64.5	120	0
14	24.4	8.5	380	0
15	25.2	17.1	276	0
16	26.2	34.1	204	0
17	25.9	63.2	171	0
18	103.3	8.3	90	0
19	100.6	16.4	90	0
20	101.3	32.4	90	0
21	102.3	63.2	90	0
22	101.5	18.2	143	2.9
23	103.4	62.1	91	2.9
24	103.5	8.7	126	2.9
25	103.0	33.1	90	2.9
26	26.3	8.3	135	2.9
27	25.3	32.0	120	2.9
28	25.6	18.2	135	2.9
29	25.4	62.5	120	2.9

TABLE 1. The experimental conditions for gravity currents generated by a sustained source of saline fluid.

those situations where the particles are vertically well-mixed and those where there exists a significant stratification. Thus, increasing the average diameter of the particles without increasing the rate of stirring indicates that it will be more difficult to maintain a well-mixed reservoir. This interpretation is fully in accord with our observations.

As a final check on the volume fraction of particles within the fluid, we drained the reservoir at the end of each experiment and weighed the unused suspension. We were thus able to calculate the mass of the suspension delivered throughout the known duration of each experiment. We also determined the concentration of particles within the remaining suspension. In all of the experiments reported here and listed in tables 1 and 2, apart from Experiments 12 and 34, this residual concentration was within 5 % of the initial bulk concentration (and for Numbers 12 and 34 the final concentration was within 10 % of the initial concentration). The average flow rate was generally well within 5 % of its initial value, apart from those runs with the lowest initial flows rates ($Q \approx 25\,\mathrm{cm^3\,s^{-1}}$, Experiments 13, 34, 30, 42), for which a somewhat larger deviation was noted.

During each of the experimental runs, measurements were made of the horizontal distance of the extremities of the current from the release point in both the downstream (X_d) and upstream (Y_u) directions as functions of time by marking the position of the nose of the current at 3 s intervals. In the case of particle-driven gravity currents, the final distribution of the sedimented particles was also measured by recovering the mass of particles within a 5 cm wide strip across the width of the tank at various distances from the release point.

Experiment number	Volume flux Q ($cm^3\,s^{-1}$)	Reduced gravity g' ($cm\,s^{-2}$)	Settling velocity v_s ($cm\,s^{-1}$)	Duration D (s)	Ambient flow speed $\overline{U}$ ($cm\,s^{-1}$)
10	52.5	33.3	0.123	240	0
11	50.8	33.3	0.123	240	2.9
12	103.9	33.3	0.123	164	2.9
13	25.6	33.3	0.123	510	2.9
30	24.6	16.8	0.123	270	2.9
31	50	16.8	0.123	240	2.9
32	104.1	16.8	0.123	165	2.9
33	49	65.6	0.123	225	2.9
34	27.5	65.6	0.123	315	2.9
35	49.1	33.3	0.056	225	0
36	49.2	33.3	0.056	240	2.9
37	48.9	33.3	0.308	240	2.9
38	51.2	33.3	0.035	225	2.9
39	103.9	33.3	0.123	240	0
40	51.4	16.8	0.123	225	0
41	49.9	65.6	0.123	225	0
42	24.5	33.3	0.123	330	0
43	50	33.3	0.308	225	0

TABLE 2. The experimental conditions for gravity currents generated by a sustained source of particle-laden fluid.

The complete list of the experimental conditions undertaken during this study is given in tables 1 and 2. In the following subsections, and throughout the rest of the paper, we describe the motion of those currents driven by salinity differences separately from those driven by suspended particles. Observations of both types of gravity current reveal that their dynamics have many common aspects. The main difference, however, is that particle settling progressively reduces the density difference between the intruding and surrounding fluids and exerts a significant control on the motion.

2.2. *Compositionally driven currents*

Compositionally driven currents of different initial densities were released from the reservoir into the ambient flow at rates in the range 25–100 $cm^3\,s^{-1}$, the density of the intruding fluid being generated by dissolving a known mass of salt (150–2400 g) into 12 l of water. (This resulted in initial values of the reduced gravity, $g^1 \equiv \Delta\rho g/\rho_a$, where g denotes gravitational acceleration, ρ_a the density of water in the Flume and $\Delta\rho$ the density difference between the intruding and ambient fluids, ranging from 8.3 to 64.5 $cm\,s^{-2}$.) Solutions of each concentration were also released into a quiescent ambient for comparison. Measurements of the upstream and downstream position of the front, as functions of time, are presented in figure 2.

In figure 2(a, b) we observe that in the absence of an ambient flow, the dense, saline fluid spreads symmetrically away from the point of release with an approximately constant speed of propagation. The rate of spreading increased as both the initial density of the intruding fluid (figure 2a) and the rate at which it was delivered to the flume (figure 2b) were increased. Whilst the motion around the head of the gravity current was unsteady with coherent billowing flow structures, similar to those reported by many previous investigators (see, for example, Simpson 1997), the bulk of the flow behind the front, but away from the source, formed a intruding layer with an approximately constant depth along the flow.

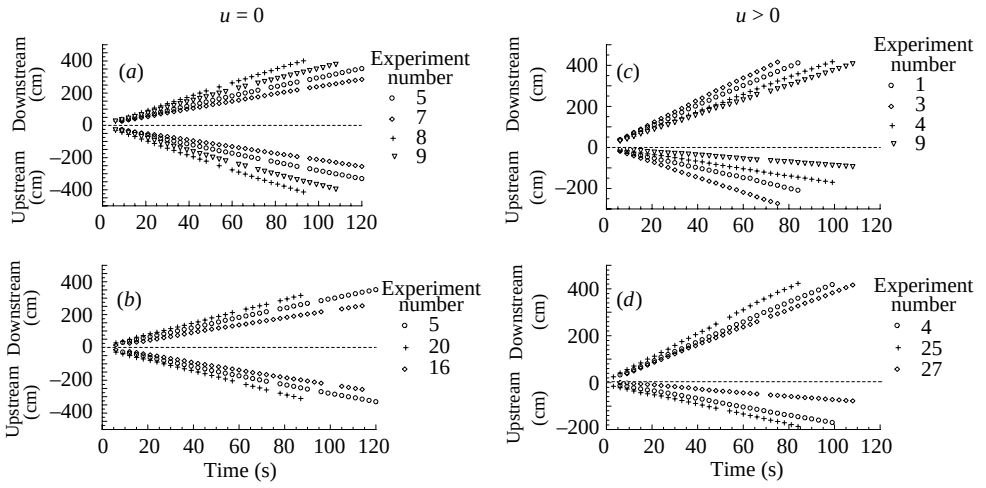

FIGURE 2. The position of the front of the saline current as a function of time: (*a*) no ambient flow, constant volume flux, varying reduced gravity; (*b*) no ambient flow, constant reduced gravity, varying volume flux; (*c*) ambient flow, constant volume flux, varying reduced gravity; and (*d*) ambient flow, constant reduced gravity, varying volume flux.

In the presence of an ambient flow, the gravity currents still spread at constant rates away from the source, although the downstream and upstream speeds are different. The nature of interface between the two fluids is rather different upstream and downstream. Downstream of the source the dense fluid deepens and maintains a characteristic head structure. In contrast, the upstream-advancing part of the current develops a wedge-like shape that is intermittently eroded by the action of interfacial eddies. Although there was some evidence of mixing between the two fluids of differing densities, the dense fluid was not vertically mixed throughout the entire water column.

2.3. *Particle-driven currents*

The particle-driven currents were generated by releasing suspensions of silicon carbide particles into the ambient flow at rates in the range 25–100 $\mathrm{cm^3\,s^{-1}}$. The silicon carbide particles have a density $\rho_p = 3.2\,\mathrm{g\,cm^{-3}}$ and we employed samples which were relatively monodisperse with mean diameters of 17, 23, 37 and 53 μm. To each suspension we added a small quantity of Calgon to prevent particle agglomeration. The initial volume concentration of particles was in the range 0.8 %–3 %, which yielded initial values of the reduced gravity, g', in the range 16–65 $\mathrm{cm\,s^{-2}}$. Upon release, the particle-driven gravity currents propagated with decreasing velocity in both the upstream and downstream directions, simultaneously depositing a sediment layer over the floor of the channel. Apart from directly under the source, where the dense plume impinged upon the base of the channel, this deposit was not changed by the subsequent flow. Figure 3 is a photographic image of a typical experiment with a particle-driven gravity current. The photograph shows the initial phases of the motion during which the dense fluid impinges upon the channel boundary and begins to propagate both upstream and downstream.

Measurements of the upstream and downstream position of the front, as a function of time, are presented in figure 4(*a–f*). When there is no mean flow in the ambient fluid, the particle-laden currents spread symmetrically away from the source (figure 4*a–c*). However in contrast to the flows of saline fluid, the speed of the propagation progressively diminishes as the particles settle out of suspension and reduce the

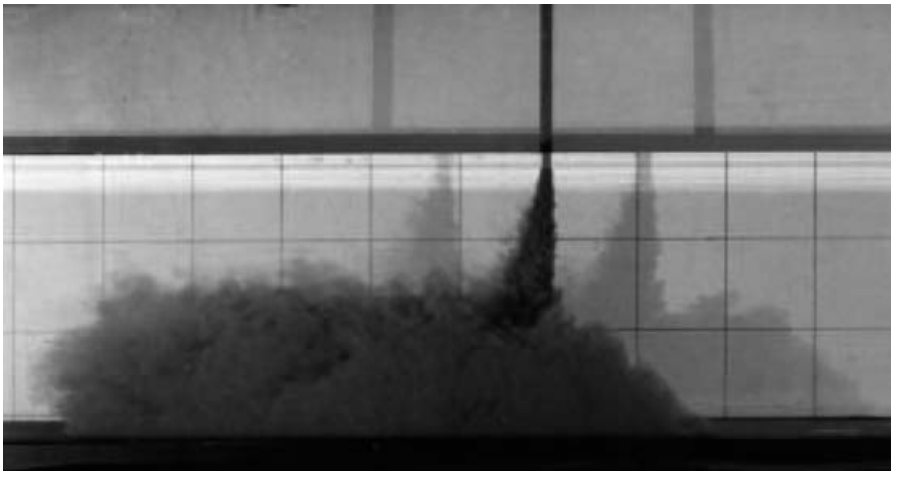

FIGURE 3. Photograph of the initial devlopment of a particle-driven gravity current in the presence of a mean flow. In this photograph the dense fluid has just impinged upon the base of the channel and started to spread up- and downstream. The mean flow is from right to left and the grid comprises squares with sides of length 10 cm.

density difference that drives the motion. Increasing the initial flux of fluid (figure 4*a*) or the initial concentration of suspended particles (figure 4*b*) increases the speed of the motion. Varying the size of the particles in suspension (and consequently varying their settling velocity) while maintaining the same initial concentration and volume flux, does not affect the rate of spreading initially (figure 4*c*). At later times though, a greater proportion of the larger particles have settled out of the flow and thus the density and speed are reduced more rapidly.

Similar systematic variations with the initial volume flux (figure 4*d*), the initial concentration of particles (figure 4*e*) and the settling velocity of the particles (figure 4*f*) are found when there is a mean flow in the ambient. All of these results indicate a substantial asymmetry in the upstream and downstream propagation of the flow. As with compositional currents, the visual appearance of the two branches is rather different: the downstream branch is somewhat diffuse, while the upstream branch forms a wedge shape, which in some runs was almost arrested by the ambient flow. There is also some evidence of mixing between the ambient and the particle-laden fluids, but this is of insufficient strength to mix the particles throughout the entire water depth.

Once the experiment was finished, the channel was partially drained and the basal deposit was sampled to determine its distribution. This was carried out by vacuuming up the sediment through a siphon tube within a $5\,\mathrm{cm} \times 25\,\mathrm{cm}$ pastry cutter placed over the bed at specific intervals. The mixture collected was then decanted and the particles dried and weighed to calculate the mass of deposit per unit area. Examples of these distributions are discussed in detail later in this paper and are plotted in figures 15 and 17. The total mass delivered during the experiment was calculated by integrating the area under these profiles of the deposit and then multiplying by the width of the channel. In each case this value was within 2 % of the measured net mass of particles delivered from the reservoir into the flume. Given the duration of each experiment and the rate at which the dense fluid enters the channel, we could also determine the average volume fraction of particles, which in each case compared favorably with the initial volume fraction.

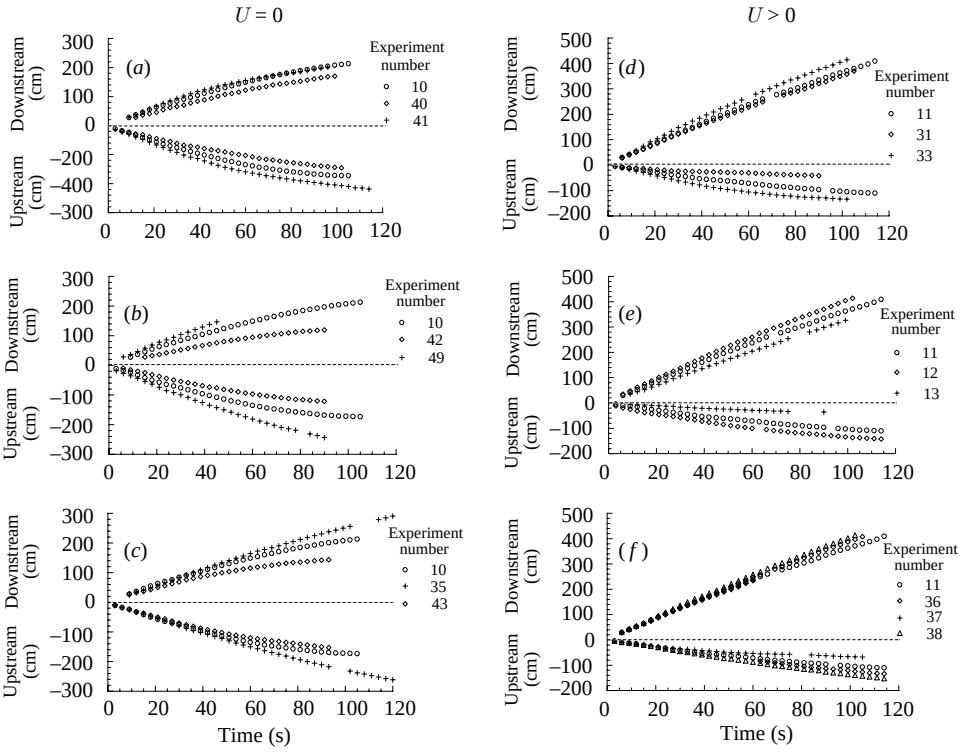

FIGURE 4. The position of the front of the particle-driven currents as a function of time. (*a*) No ambient flow, constant volume flux and settling velocity, varying initial concentration of particles. (*b*) No ambient flow, constant initial concentration of particles and settling velocity, varying volume flux. (*c*) No ambient flow, constant initial concentration of particles and volume flux, varying settling velocity. (*d*) Ambient flow, constant volume flux and settling velocity, varying initial concentration of particles. (*e*) Ambient flow, constant initial concentration of particles and settling velocity, varying volume flux. (*f*) Ambient flow, constant initial concentration of particles and volume flux, varying settling velocity.

A noteworthy sedimentological feature of these experimental results was the formation of ring-like structures within the deposited sediment, centred directly beneath the source where the particle-laden fluid impinges upon the underlying boundary. Typically there were two concentric ridges of sediment raised above the surrounding and relatively flat deposit. Such structures were formed in both quiescent conditions and in the presence of a mean flow. In the former case, the ridges were approximately circular. (For an input flux of $52\,\mathrm{cm^3\,s^{-1}}$ and initial volume fraction of 4.7 %, the diameter of the inner ring was 13 cm and the outer ring 17 cm.) In the presence of a mean flow the rings were extended downstream and were elliptical.

2.4. *Entry conditions and initial mixing*

The dense fluid flowed from the elevated reservoir through a pipe of cross-sectional area $A = 0.50\,\mathrm{cm^2}$, which was held 5 mm under the free surface of the ambient fluid. Thereafter it descended through the ambient, where it entrained fluid and was then deflected by the bottom of the channel so that the dense fluid propagated both up- and downstream with approximately equal fluxes of fluid supplied in each direction.

During the descent phase, the motion of dense fluid was dynamically intermediate between jet- and plume-like behaviour and was strongly modified by the presence of

the underlying boundary and the sidewalls of the flume. Previous investigations of this type of flow include Linden & Simpson (1990, 1994), Gilmour & Woods (1994) and Cavalletti & Davies (2003). While the experimental configuration in each of these studies is different from that employed here, we also measure the degree of dilution of the source fluid (the mixing with the ambient) as a function of the ratio of the depth of the ambient to the jet length of the input fluid. Importantly we note that provided there is only negligible particle settling during this interaction then the buoyancy of the flow is conserved under mixing.

The initial specific momentum flux of the plume, M_0, has dimensions L^4T^{-2}, while the initial specific buoyancy flux, B_0 has dimensions L^4T^{-3}. Hence the lengthscale constructed from these two, known as the jet length, is given by $M_0^{3/4}B_0^{-1/2}$. Relating these to the initial volume flux, Q_0, the reduced gravity at the source, g', and the cross-sectional area of the source, A we find that the jet length is proportional to $Q_0 g'^{-1/2}A^{-3/4}$. Finally, the volume flux per unit width is given by $q_p = Q_0/w$, where w is the width of the channel. Thus in this series of experiments for which both w and A remain constant, the jet length is proportional to the buoyancy lengthscale $h_b = (q_p^2/g')^{1/3}$.

In an unbounded fluid, it is possible to employ simple dimensional reasoning to show that at a distance z from the source, the volume flux is proportional to $M_0^{1/2}z$, when z is much less than the jet length, and to $B_0^{1/3}z^{5/3}$, when z is much greater than the jet length (Morton, Taylor & Turner 1956; Turner 1973). Thus we expect that the increase in the volume flux relative to its initial value, Q/Q_0, to be proportional to $H/A^{1/2}$ when $H \ll h_b$ and to $H^{5/3}/[h_b w^{2/3}]$, when $H \gg h_b$. We develop below an empirical expression for the volume flux generated by the method of dense fluid release employed in these experiment. This expression is constrained to be consistent with this dimensional reasoning when the depth of the fluid, H, is either much smaller, or much greater, than the buoyancy lengthscale, h_b.

We performed a series of experiments (see § 2.2) in which solutions of dense saline fluid were released into the channel in the absence of an ambient flow. The dense fluid spread along the underlying channel boundary at a constant speed, u, and formed a moving layer of constant depth, h. From the velocity and density profiles of flowing gravity currents, measured by Ellison & Turner (1959), Buckee, Kneller & Peakall (2001), Kneller, Bennett & McCaffrey (1999), Altinakar, Graf & Hopfinger (1996) and calculated by Simpson & Britter (1979) and Felix (2002), we estimate that the volume flux carried by this flowing layer is given by $Q_i = 0.6uhw$. We henceforth seek an empirical relationship between this volume flux, measured in our experiments relative to the volume flux at the source and the ratio of the fluid depth H to the buoyancy lengthscale h_b (figure 5). We note that the proposed linear relationship has the correct form in the regimes $H/h_b \gg 1$ and $H/h_b \ll 1$ and that the best-fit curve is given by

$$Q_i/Q_0 = 0.048\frac{H}{h_b} + 6.8. \tag{2.1}$$

We also empirically find that

$$h/H = 10.0\frac{h_b}{H} + 0.041. \tag{2.2}$$

This form is consistent with the expression for the flux (2.1) if the velocity, u, is proportional to $(g'q_p)^{1/3}$.

In the absence of particle settling, the buoyancy flux is conserved under mixing and thus (2.1) provides a means for calculating the reduced gravity of the flow. For

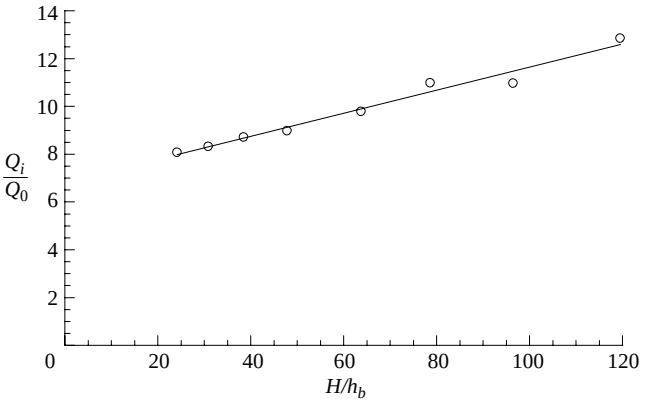

FIGURE 5. The increase in the volume flux relative to the initial volume flux, Q_i/Q_0, measured as a function of H/h_b.

compositionally driven currents, it will be established below that the velocity depends only on the buoyancy flux per unit width and thus there is no need to employ this empirical expression for the mixing. However, for particle-driven flows it will be shown that it is necessary to calculate both the initial concentration of particles and volume flux. For these flows the measured speed of the current and the distribution of the deposited particles form an independent verification of the empirical expression for the dilution.

3. Shallow-water models

Shallow-water models of hydraulics phenomena are formulated on the assumption that the horizontal lengthscale of the motion far exceeds the vertical lengthscale so that vertical accelerations are negligible and the pressure is hydrostatic to leading order (see, for example, Whitham 1974). This class of model has been widely used in contexts as diverse as coastal dynamics (Peregrine 1972), river and estuarine mechanics (Parker 1976), debris flows (Iverson 1997) and avalanches (Hopfinger 1983). Furthermore a number of recent studies have employed this framework to analyse the propagation of gravity currents and have demonstrated that the depth-averaged equations may be used to provide accurate predictions of the motion (see, for example Rottman & Simpson 1983; Bonnecaze *et al.* 1993 and Hallworth *et al.* 1998).

The depth of a flowing gravity current is often much less than the environment through which it is propagating and so it is often possible to neglect the motion induced within the ambient. In this study such an assumption may not be appropriate since the depth of the currents was in some experiments in excess of a third of the depth of the ambient. Furthermore we observed that the profile of the current was dependent upon whether its direction of motion was up- or downstream. We also noted that at late stages of the motion there was an intermediate layer within which the gravity current and ambient fluids mixed. This region remained localized and dense fluid was not observed to be mixed throughout the entire water column.

Multi-layer hydraulic models have received considerable attention during recent years, being applied to the problem of exchange flows between locks, or reservoirs, which contain fluids with different densities. The motion between these different fluids may progress over a sill or through a constriction, and this topography exerts a significant control over the possible types of flows. Various techniques have been employed

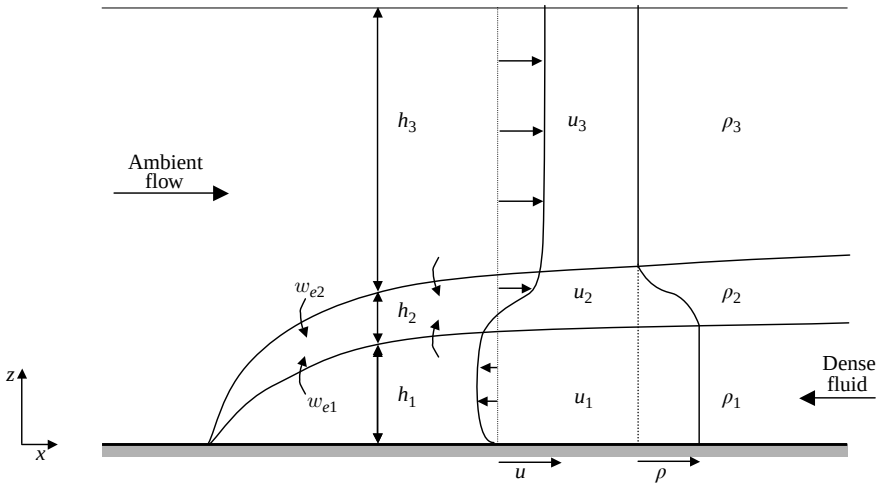

FIGURE 6. The configuration of the theoretical model of the flow.

to analyse the steady exchanges that may occur. These include: the specification of 'hydraulic control' in terms of Froude numbers for each layer (Armi & Farmer 1986; Baines 1988); the derivation of an hydraulic functional within which transitions occur between different branches of solution (Dalziel 1991); and a variational principle in which the horizontal flow force is maximal at control points (Benjamin 1981). Generally these hydraulic models take no account of mixing between the fluid layers of differing densities, nor of interfacial friction. Notable exceptions include Anati, Assaf & Thompson (1977) who identified the lengthscale over which frictional effects may become significant and Zhu & Lawrence (2000) who showed that drag may alter the position of control points.

Estuarine salt wedges share many dynamical features with saline gravity currents which propagate against a mean flow. Dynamical models of salt wedges were first formulated by Schijf & Schönfeld (1953), who studied a two-layer model of a salt wedge in which the pressure gradient associated with the excess density of the saline fluid was balanced by the interfacial drag between the arrested basal layer and over-riding river flow. This approach was generalized by Arita & Jirka (1987*a*) who permitted the lower layer to be in motion and accounted for the mixing between the two fluids. Finally, Sorgard (1991) formulated a three-layer model, consisting of a dense basal layer, an interfacial layer of intermediate density and an overflowing layer of relatively low density. In this model there is drag and entrainment at the interface between each of the layers, although Sorgard (1991) further assumed that the density of the intermediate layer remains constant and this places a strong constraint on the magnitude of the entrainment between the layers.

In this study, we formulate a three-layer model of the motion (see figure 6). There are no topographic constraints, such as sills or constrictions, and we examine the possibility that at late times of the motion, mixing and drag between the layers may be of considerable importance. As we demonstrate below, most of the experimental observations are at time- and lengthscales before drag strongly influences the motion. However this framework provides a consistent way in which the entire motion can be modelled. It also emphasizes the dynamic similarities between the intrusion of saline gravity currents and estuarine salt wedges.

The configuration of the flow is sketched in figure 6. The upper layer is assumed to consist of fresh water of density ρ_3. The basal layer comprises dense fluid, due either to compositional differences or to the presence of suspended particles. We denote the density of this lowest layer by ρ_1. If the current is due to compositional differences then the density of this layer remains unchanged; however if there are suspended particles then sedimentation reduces the density. In between these two there is a layer of density between ρ_1 and ρ_3. This layer, and its density, evolves due to mixing with the under- and overlying fluids. We assume that the difference in density between the upper and lower layers is relatively small $[(\rho_1 - \rho_3)/\rho_3 \ll 1]$, so that the dynamics may be treated using the Boussinesq approximation. Furthermore we assume that the Froude number of the background flow is also small, $\overline{u}/\sqrt{gH} \ll 1$, where H is the depth of the ambient fluid, g gravitational acceleration and $\overline{u}$ the mean ambient flow speed. This implies that we may assume that the total depth of the fluid remains constant (the rigid lid approximation). Thus denoting the height of each layer by h_i,

$$h_1 + h_2 + h_3 = H. \tag{3.1}$$

In these experiments, $(\rho_3 - \rho_1)/\rho_1 \approx 0.05$ and $\overline{u}/\sqrt{gH} \approx 0.02$ so that these constraints are comfortably satisfied. We note though that an equivalent theory could be developed without these simplifications.

We chose the coordinate axes (x, z) such that z is vertical and x is horizontal down the channel. The horizontal velocity field within each layer is denoted by u_i and, using the Boussinesq approximation, mass conservation within the channel is given by

$$\int_0^{h_1} u_1 \,\mathrm{d}z + \int_{h_1}^{h_1+h_2} u_2 \,\mathrm{d}z + \int_{h_1+h_2}^{H} u_3 \,\mathrm{d}z = H\overline{u}. \tag{3.2}$$

We may also account for the mixing between the layers and thus model the evolution of the volume fluxes carried by each of the layers. We represent this mixing processes by entrainment at which velocities that are rates per unit area that volumes of gravity current and ambient fluids are mixed into the intermediate layer from the adjoining layers. These entrainment velocities for the mixing from the dense gravity current and from the ambient fluid into the intermediate layer are denoted by w_{e1} and w_{e2}, respectively, and thus we find that

$$\frac{\partial h_1}{\partial t} + \frac{\partial}{\partial x}\left(\int_0^{h_1} u_1 \,\mathrm{d}z\right) = -w_{e1}, \tag{3.3}$$

$$\frac{\partial h_2}{\partial t} + \frac{\partial}{\partial x}\left(\int_{h_1}^{h_1+h_2} u_2 \,\mathrm{d}z\right) = w_{e1} + w_{e2}. \tag{3.4}$$

As a consequence of the shallow-water approximation, the pressure, p, adopts hydrostatic distributions in each of the layers, given by

$$p = \begin{cases} p_0(x) + \rho_3 g(H - z), & h_1 + h_2 < z \leqslant H, \\ p_0(x) + \rho_3 g h_3 + \rho_2 g(h_1 + h_2 - z), & h_1 < z \leqslant h_1 + h_2, \\ p_0(x) + \rho_3 g h_3 + \rho_2 g h_2 + \rho_1 g(h_1 - z), & 0 < z \leqslant h_1, \end{cases} \tag{3.5}$$

where $p_0(x)$ is the pressure at the surface $z = H$. Henceforth we measure the density differences between the layers in terms of the reduced gravity for each layer, given by

$$g_i' = (\rho_i - \rho_3)g/\rho_3 \qquad (i = 1, 2). \tag{3.6}$$

The flow is driven by horizontal pressure gradients arising from the density differences between the fluids. Therefore the expressions for the depth-integrated horizontal

momentum for each layer are

$$\frac{\partial}{\partial t}\left(\int_{h_1+h_2}^{H} u_3\,\mathrm{d}z\right)+\frac{\partial}{\partial x}\left(\int_{h_1+h_2}^{H} u_3^2\,\mathrm{d}z\right)+\int_{h_1+h_2}^{H}\frac{1}{\rho_3}\frac{\partial p}{\partial x}\,\mathrm{d}z=-\frac{F_{23}}{\rho_3}-w_{e2}u_3|_{h_1+h_2}, \quad (3.7)$$

$$\frac{\partial}{\partial t}\left(\int_{h_1}^{h_1+h_2} u_2\,\mathrm{d}z\right)+\frac{\partial}{\partial x}\left(\int_{h_1}^{h_1+h_2} u_2^2\,\mathrm{d}z\right)+\int_{h_1}^{h_1+h_2}\frac{1}{\rho_3}\frac{\partial p}{\partial x}\,\mathrm{d}z$$
$$=\frac{F_{23}-F_{12}}{\rho_3}+w_{e2}u_2\big|_{h_1+h_2}+w_{e1}u_2\big|_{h_1}, \quad (3.8)$$

$$\frac{\partial}{\partial t}\left(\int_{0}^{h_1} u_1\,\mathrm{d}z\right)+\frac{\partial}{\partial x}\left(\int_{0}^{h_1} u_1^2\,\mathrm{d}z\right)+\int_{0}^{h_1}\frac{1}{\rho_3}\frac{\partial p}{\partial x}\,\mathrm{d}z=\frac{(F_{12}-F_b)}{\rho_3}-w_{e1}u_1|_{h_1}, \quad (3.9)$$

where F_{ij} denotes the interfacial shear stress between layers i and j, F_b denotes the basal shear stress, $u_i|_z$ denotes the velocity $u_i(x,z)$. In (3.7) the shear stress at the free surface has been assumed to be negligible. Basal drag may substantially modify the flow of gravity currents (Hogg & Woods 2001). However in this study we assume that its magnitude is negligible relative to the interfacial drag and henceforth we omit it from the governing equations.

Finally we express the evolution of the densities of the mixed and basal layers. If the density is solely due to compositional differences then it may only vary due to mixing processes between the two layers. However if it is due to the presence of suspended sediment then it will be progressively reduced by particle settling. In this study we have examined those gravity currents that are either solely driven by the compositional differences or solely by the suspended particulate. It is thus possible to formulate expressions that model the evolution of the reduced gravity of each layer; saline currents may then be treated by imposing a vanishing settling velocity. Therefore the reduced gravity of each layer evolves according to

$$\frac{\partial}{\partial t}\int_{0}^{h_1} g_1'\,\mathrm{d}z+\frac{\partial}{\partial x}\left(\int_{0}^{h_1} g_1'u_1\,\mathrm{d}z\right)=-v_s g_1'|_0+v_s g_3'|_{h_1}-w_{e1}g_1'|_{h_1}, \quad (3.10)$$

$$\frac{\partial}{\partial t}\int_{h_1}^{h_1+h_2} g_2'\,\mathrm{d}z+\frac{\partial}{\partial x}\left(\int_{h_1}^{h_1+h_2} g_2'u_2\,\mathrm{d}z\right)=-v_s g_3'|_{h_1}+w_{e1}g_1'|_{h_1}, \quad (3.11)$$

where $g_i'|_z\equiv g_i'(x,z)$. It is assumed that particles which have been deposited from the flow are not re-entrained. It is further assumed that the turbulence is sufficient to maintain a uniform suspension throughout the entire fluid layer (Martin & Nokes 1988; Bonnecaze *et al.* 1993; Hallworth *et al.* 1998). We return to this issue in § 5.

The depth-integrated model is simplified by assuming that the the velocity and density fields are piecewise constant within each of the layers. This is an approximation, which lies at the heart of many 'hydraulic' models and most shallow-layer modelling of gravity currents. Some investigators have assumed instead that the velocity and density fields have a self-similar form, which permits the evaluation of these vertical integrals, and yields a series of somewhat arbitrary 'shape' factors that specify the self-similar form. Generally the neglect of these shape factors introduces little error into the one-dimensional model (although see Hogg & Pritchard (2004), who show that the theoretical speed of dambreak flow is strongly dependent upon the magnitude of these shape factors).

Finally, in order to close the model we specify the interfacial stresses and entrainment velocities. These quantities are related and may be expected to be functions of the velocity and density gradients across the interface, as well as depending strongly upon

the structure and nature of the turbulent fluctuations. Arita & Jirka (1987*a*, *b*) and Sorgard (1991) discuss possible empirical expressions for these processes and review of some the laboratory measurements of them. In this study, following Sorgard (1991), we adopt simple models for the stresses and entrainment fluxes, noting that more elaborate closures could be readily employed. We write the interfacial stresses as

$$F_{23} = C_{D2}\rho_3(u_3 - u_2)|u_2 - u_3|, \qquad F_{12} = C_{D1}\rho_3(u_2 - u_1)|u_2 - u_1|, \tag{3.12}$$

where C_{D1} and C_{D2} are constant drag coefficients. Further, the entrainment velocities are assumed to be given by

$$w_{e1} = E_1|u_1 - u_2|, \qquad w_{e2} = E_2|u_2 - u_3|, \tag{3.13}$$

where the entrainment coefficients, E_1 and E_2 are also assumed to be constant. Typical magnitudes of these entrainment and drag coefficients are 10^{-2}, although they are functions of the Reynolds and Froude numbers of the flow (Arita & Jirka 1987*a*).

The gravity currents studied in the experiments of § 2 were generated by the impingement of an initially vertical plume on a horizontal boundary and its subsequent deflection and propagation away from the source. During this impingement a shallow-water model of the flow is not appropriate because there is no separation in lengthscales between the vertical and the horizontal and the pressure is not hydrostatic. However, at some distance from the source ($x = \pm\Delta$, where $\Delta \approx 30$ cm in the present case), the flow has become predominantly horizontal and so the mathematical formulation presented above may be employed. Since the flow is subcritical, as will be shown empirically below, we need only specify the volume flux per unit width and the buoyancy flux per unit width. Hence on the assumption that the descending plume delivers equal fluxes both upstream and downstream, we require that

$$u_1 h_1 = -q/2, \; u_1 g_1' h_1 = -q g_0'/2 \qquad \text{at } x = -\Delta, \tag{3.14}$$

$$u_1 h_1 = q/2, \; u_1 g_1' h_1 = q g_0'/2 \qquad \text{at } x = \Delta, \tag{3.15}$$

where q is the volume flux per unit width and g_0' is the initial reduced gravity.

At the front of the current, during the initial propagation the motion is unsteady and three-dimensional as the dense fluid propagates through and displaces ambient fluid. Such fluid motion cannot be modelled using the shallow-water equations. Instead we invoke the Froude number condition (Benjamin 1968; Huppert & Simpson 1980), supplemented by the uniform flow (Simpson & Britter 1980; Hallworth *et al.* 1998). Thus we write

$$u = U + Fr(g'h)^{1/2} \qquad \text{at } x = X_d(t), \tag{3.16}$$

$$u = U - Fr(g'h)^{1/2} \qquad \text{at } x = -X_u(t), \tag{3.17}$$

where $X_d(t)$ and $X_u(t)$ are the positions of the front of the current in the downstream and upstream directions, respectively, u and h are the velocity and depth of the dense fluid at the front and Fr is the Froude number at the front of the flow. Here the velocity U is that experienced by the gravity current due to the mean flow. Previous studies (Simpson & Britter 1980; Bühler, Wright & Kim 1992; Hallworth *et al.* 1998) have shown empirically that the speed of the gravity current is equal to the density-driven speed in the absence of a mean flow, plus a fraction approximately 0.6 of the mean uniform flow. The Froude number is a function of the depth at the front of the current relative to the depth of the ambient (see, for example, Huppert & Simpson 1980). However provided the current is deep relative to the ambient, the Froude number is approximately constant.

These conditions at the front of the current are formulated on the assumption that basal and interfacial drag are negligible. We do not expect that (3.16) and (3.17) will be appropriate boundary conditions when the flows have become dominated by drag. Instead, other studies have shown that in such a regime the front of the current is defined by the position at which the layer height vanishes (Hatcher, Hogg & Woods 2000; Hogg & Woods 2001).

3.1. *Non-dimensionalization*

We now recast the governing equations derived above in terms of dimensionless variables. Although there are a number of length- and timescales in this flow, it is convenient to render the variables dimensionless using the lengthscale $(q^2/g_0')^{1/3}$ and the timescale $(q/g_0'^2)^{1/3}$ and henceforth, unless stated to the contrary, all variables will be assumed to be dimensionless. The dimensionless expressions for the total depth of the fluid and the total flux within the channel are then given by

$$h_1 + h_2 + h_3 = \mathscr{H}, \tag{3.18}$$

$$h_1u_1 + h_2u_2 + h_3u_3 = \mathscr{H}\mathscr{U}, \tag{3.19}$$

where $\mathscr{H} = (g_0'/q^2)^{1/3}H$ and $\mathscr{U} = \overline{u}/(g_0'q)^{1/3}$. Mass conservation within the lower two layers is given by

$$\frac{\partial h_1}{\partial t} + \frac{\partial}{\partial x}(u_1h_1) = -E_1|u_2 - u_1|, \tag{3.20}$$

$$\frac{\partial h_2}{\partial t} + \frac{\partial}{\partial x}(u_2h_2) = E_1|u_2 - u_1| + E_2|u_3 - u_2|. \tag{3.21}$$

The horizontal momentum equation of each layer is given by

$$\frac{\partial u_1}{\partial t} + u_1\frac{\partial u_1}{\partial x} + \frac{\partial p_0}{\partial x} + \frac{\partial}{\partial x}(g_2'h_2) + \frac{h_1}{2}\frac{\partial g_1'}{\partial x} + g_1'\frac{\partial h_1}{\partial x} = \frac{C_{D1}(u_2 - u_1)|u_2 - u_1|}{h_1}, \tag{3.22}$$

$$\frac{\partial u_2}{\partial t} + u_2\frac{\partial u_2}{\partial x} + \frac{\partial p_0}{\partial x} + \frac{h_2}{2}\frac{\partial g_2'}{\partial x} + g_2'\frac{\partial}{\partial x}(h_1 + h_2) = \frac{C_{D2}(u_3 - u_2)|u_3 - u_2|}{h_2} - \frac{C_{D1}(u_2 - u_1)|u_2 - u_1|}{h_2}, \tag{3.23}$$

$$\frac{\partial u_3}{\partial t} + u_3\frac{\partial u_3}{\partial x} + \frac{\partial p_0}{\partial x} = \frac{-C_{D2}(u_3 - u_2)|u_3 - u_2|}{h_3}. \tag{3.24}$$

Finally the evolution of the buoyancy of the lower two layers is given by

$$\frac{\partial g_1'}{\partial t} + u_1\frac{\partial g_1'}{\partial x} = \frac{\mathscr{V}_s(g_2' - g_1')}{h_1}, \tag{3.25}$$

$$\frac{\partial g_2'}{\partial t} + u_2\frac{\partial g_2'}{\partial x} = -\frac{\mathscr{V}_s g_2'}{h_2} + \frac{E_1|u_2 - u_1|(g_1' - g_2') - E_2|u_2 - u_3|g_2'}{h_2}, \tag{3.26}$$

where $\mathscr{V}_s = v_s/(g_0'q)^{1/3}$. In this system of equations there are seven dimensionless parameters. These are the entrainment coefficients, E_1 and E_2, the drag coefficients, C_{D1} and C_{D2}, the dimensionless total depth of fluid, $\mathscr{H}$, the ratio of the mean flow in the ambient to velocity of the buoyancy-driven flow, $\mathscr{U}$, and the dimensionless settling velocity of the particles, $\mathscr{V}_s$.

In the absence of drag and entrainment, this three-layer model is considerably simplified; the mixed layer vanishes ($h_2 = 0$) and the model becomes identical to that used in previous investigations of saline and particle-laden gravity currents (Rottman &

Simpson 1983; Bonnecaze *et al.* 1993; Hallworth *et al.* 1998). Furthermore, in the regime $(g_0' H^3/q^2)^{1/3} \gg 1$, the dynamics of the lower layer become independent of the upper layer and thus the model reduces to a single-layer hydraulic model, which is identical to that used in many studies of the motion of gravity currents.

In subsequent sections of this paper we present solutions to this model and compare the theoretical predictions and experimental observations. However at this stage we derive simple estimates of the lengthscale, L, and timescale, T at which drag effects become significant. Following Hogg & Woods (2001) we estimate that this first occurs when the inertia and pressure gradient are comparable with the drag forces. On the assumption that the reduced gravity of the dense layer has not decreased significantly from its initial value, in dimensional terms this occurs when $g_0' h/L \sim C_{D1}\overline{u}^2/h$, where $h \sim (q^2/g_0')^{1/3}$ is a typical depth of the dense layer. Thus the lengthscale is given by $L \sim q(g_0' q)^{1/3}/[C_{D1}\overline{u}^2]$ and the timescale by $T \sim q/[C_{D1}\overline{u}^2]$. For length- and timescales less than these the effects of interfacial drag are weak. For a drag coefficient $C_D = 10^{-2}$, this lengthscale is approximately 10^3 cm for these experiments. This corresponds to the length of the flume in which the experiments were carried out and so for the compositional currents it is unlikely that significant effects of drag will be noted in the experimental results presented below; indeed we did not find experimental conditions in which the upstream propagating branch of a saline current was arrested fully by the mean flow. However, particle settling may significantly reduce the excess density of the intruding gravity current, which will shorten the lengthscale over which drag begins to influence the motion.

4. Compositionally driven gravity currents

In this section we analyse the experimental results for flows in which the density difference between the intruding and ambient fluids is solely due to differences in their composition. The density of the lowest layer is constant, therefore, and in terms of the mathematical model developed above we impose $\mathscr{V}_s = 0$. We also note that for steady flows the buoyancy flux of the lower two layers is constant, irrespective of mixing processes (i.e. $u_1 g_1' h_1 + u_2 g_2' h_2$ is constant). We first investigate flows for which the drag is negligible (§ 4.1) and find that this is sufficient to model accurately most of the experimental observations. In § 4.2 we analyse how the effects of drag and entrainment modify the motion and we derive a new three-layer model of a steady saline wedge.

4.1. *Drag-free motion*

In the absence of an ambient flow ($\mathscr{U} = 0$), we observed that the dense fluid moves away from the source symmetrically along the bottom of the channel (see § 2.2, figure 2). It forms layers of approximately constant depth and moves with approximately a constant speed. In the absence of drag and entrainment, the three-layer model developed above is considerably simplified and there are simple similarity solutions for the flow speed and height (Hoult 1972; Gratton & Vigo 1994). If the source is subcritical then the solution is given by

$$u_1 h_1 = 1, \qquad u_1 = Fr\sqrt{h_1}. \tag{4.1}$$

However if the source is supercritical then the velocity and height of the current depend upon the Froude numbers at the source and the front; the flow fields are no longer constant and may exhibit discontinuities or points of critical transition (Gratton & Vigo 1994). In these experiments the descending plume delivered the

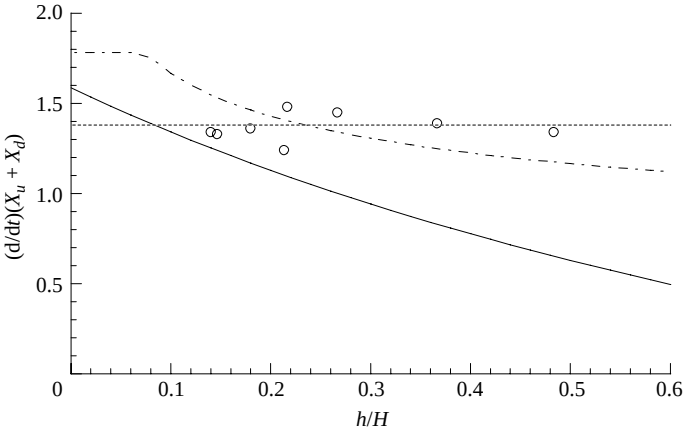

FIGURE 7. The dimensionless rate of growth of the length of the gravity current as a function of depth relative to the ambient, h/H, for the experimental data (○) and the models of Huppert & Simpson (1980) (——) and Rottman & Simpson (1983) (–·–·). Also plotted is the average value (- - - -).

dense fluid at subcritical conditions and thus the front speeds are given by

$$\frac{\mathrm{d}X_d}{\mathrm{d}t} = \frac{\mathrm{d}X_u}{\mathrm{d}t} = \left(\frac{Fr^2}{2}\right)^{1/3}. \tag{4.2}$$

We fit straight lines through plots of the length of current, $X_u + X_d$, against time to determine empirically the value of the Froude number. In figure 7, we plot this Froude number as a function of the intrusion depth relative to the depth of the ambient fluid. We find that although there is some evidence that the measured Froude number follows the formulae proposed by Huppert & Simpson (1980) and by Rottman & Simpson (1983), there is sufficient scatter in the data that for the range of conditions in this experimental series we may take the Froude number to be constant, with value $Fr = 0.81$. We note that this is in excellent agreement with the results of Linden & Simpson (1990) and Gilmour & Woods (1994).

On the assumption that the Froude number is constant, we plot the dimensionless length of the current, $(X_u + X_d)(q_p^2/g')^{-1/3}$ as a function of dimensionless time $t(q_p/g'^2)^{-1/3}$ (figure 8). Note that these scalings yield a very good collapse of the data. Further note that we have not had to take account of the mixing with the ambient which occurs on input to the channel. This is possible because the velocity scale, $(q_p g')^{1/3}$, is conserved throughout any mixing. Thus the length- and timescales are linearly scaled by the same factor when rendered dimensionless. As explained in § 5, this does not apply for a particle-driven current, because its buoyancy is progressively reduced.

In the presence of an ambient flow ($\mathscr{U} > 0$), the current no longer propagates symmetrically away from the source; rather the downstream speed is increased and the upstream speed is reduced. However the speed of propagation in either direction remains approximately constant (see figure 2). In the absence of entrainment and drag the effects of the mean flow are directly included via the conditions at the fronts of the current (3.16), (3.17), which introduce an asymmetry in the rates of spreading. As above we seek a constant solution for the velocity and height, but treat the

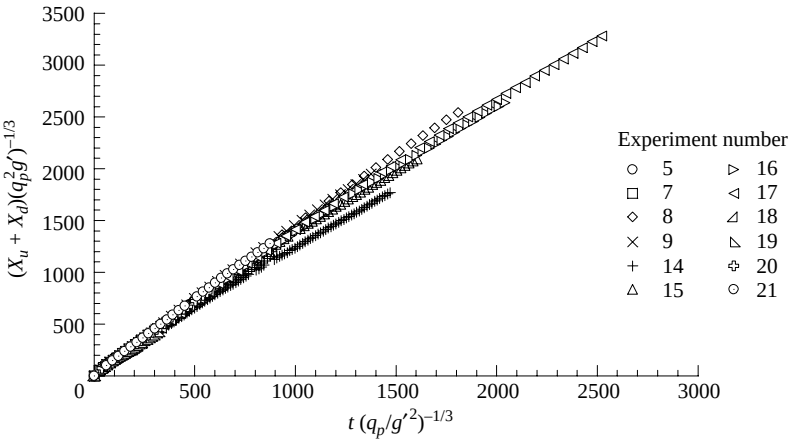

FIGURE 8. The dimensionless length of the gravity current as a function of dimensionless time. This plot includes all of the experimental data for saline currents in the absence of a mean ambient flow.

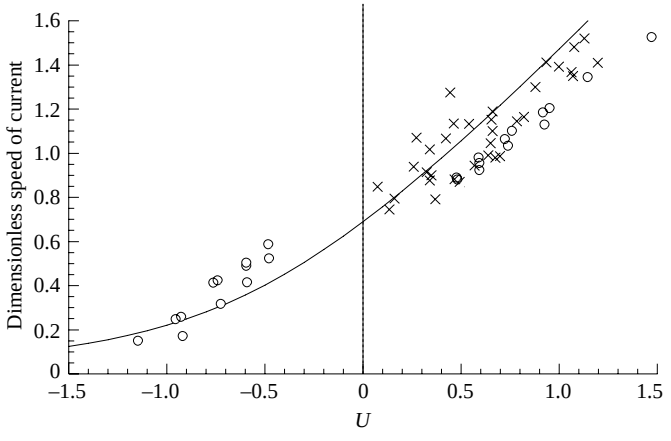

FIGURE 9. The dimensionless speed of the gravity current propagating in the presence of a mean ambient flow as a function of the dimensionless strength of the ambient flow. ○, This study; ×, data from Bühler *et al.* (1991).

upstream and downstream branches separately. Thus we write

$$\frac{\mathrm{d}X_u}{\mathrm{d}t} = \alpha, \qquad \frac{\mathrm{d}X_d}{\mathrm{d}t} = \beta, \tag{4.3}$$

where α and β satisfy

$$\alpha = \mathscr{U} + Fr(2\alpha)^{-1/2}, \qquad \beta = -\mathscr{U} + Fr(2\beta)^{-1/2}, \tag{4.4}$$

where we have assumed that the velocity U is equal to the mean flow $\overline{u}$. We fit best-fit lines through the graphs of both $X_u(t)$ and $X_d(t)$ as functions of time to determine the experimental values of α and β. On the assumption that the Froude number is constant and equal to 0.81 (as determined above) and that the velocity experienced by the current is equal to the mean ambient flow, we compare the theoretical predictions of (4.4) with the experimental measurements (figure 9). We find that the comparison is reasonably good, apart for those currents which are propagating upstream against

a relatively strong ambient flow and move slower than predicted. A possible reason for this difference is that such flows are influenced by the action of interfacial drag between the slowly moving dense fluid layer and the overlying, relatively rapid, ambient flow. Also in figure 9, we plot data from the experiments of Bühler *et al.* (1991), in which saline solutions were released with a co-flowing ambient.† We note that the two data sets are consistent and are reasonably well modelled by this the simple theory.

We evaluate the rates of upstream and downstream propagation in the regime $\mathscr{U} \ll 1$ to find that

$$\alpha = \left(\frac{Fr^2}{2}\right)^{1/3} + \frac{2\mathscr{U}}{3} + \ldots, \qquad \beta = \left(\frac{Fr^2}{2}\right)^{1/3} - \frac{2\mathscr{U}}{3} + \ldots. \tag{4.5}$$

Thus when the mean flow is much less than the buoyancy velocity scale, we find that to first order, the speed of the gravity current is equal to the speed of the density-driven motion in the absence of the mean flow plus 2/3 of the mean flow. This is of a similar form to the empirical rule proposed by Simpson & Britter (1980). Conversely, in the regime $\mathscr{U} \gg 1$, we find that

$$\alpha = \mathscr{U} + \frac{Fr}{(2\mathscr{U})^{1/2}} + \ldots, \qquad \beta = \frac{Fr^2}{2\mathscr{U}^2} - \frac{Fr^4}{2\mathscr{U}^5} + \ldots. \tag{4.6}$$

Thus we note that in this regime of a strong mean flow, the downstream flow speed becomes asymptotically equal to the mean flow speed, while the upstream flow speed becomes small $O(\mathscr{U}^{-2})$.

4.2. *Drag-affected motion*

It was established above that the effects of drag become dominant after the current has propagated for a sufficient time, given in dimensionl units by $t \gg q/[C_{D1}\overline{u}^2]$. The experiments were thus in a regime that precluded observation of this transition. In this subsection we examine theoretically the effects of drag on the upstream propagating current and calculate some of the predictions of the model derived in § 3. We establish a new dynamical regime in which the buoyancy forces balance the interfacial drag and show that the speed is slowed. We also show that by including entrainment between the three layers, a steady arrested state may be determined.

First we consider motion through a sufficiently deep ambient fluid ($h_1, h_2 \ll h_3$) that the flow speed of the upper layer can be assumed constant and we employ scaling analysis to assess the magnitudes of the forces on the current. The initial motion arises from a balance between the pressure gradient associated with the excess density and the fluid inertia. Thus in the lower layer, $u_1^2 \sim h_1$, and since the current is driven by a constant flux of dense fluid, $u_1 h_1 \sim 1$, we deduce that $u_1 \sim 1$ and the length of the current increases as t. Drag forces are of magnitude $C_{D1}\mathscr{U}^2/h_1$ and are initially negligible. However when $t \gg 1/[C_{D1}\mathscr{U}^2]$, they become non-negligible and balance the streamwise pressure gradient associated with the difference in density, with the inertia becoming negligible. An analogous transition in dynamical behaviour was found for currents affected by basal drag (Hogg & Woods 2001). The thickness of the intermediate mixed layer is assumed to be small relative to depth of the lower layer, $h_2 \sim E_2\mathscr{U}t \ll h_1$. Thus in this regime, conservation of mass is given by (3.20) and

† Because the experimental configuration is different from that reported here, we determine the mean velocity, $\overline{u}$, as the total volume flux in the channel divided by the flow depth.

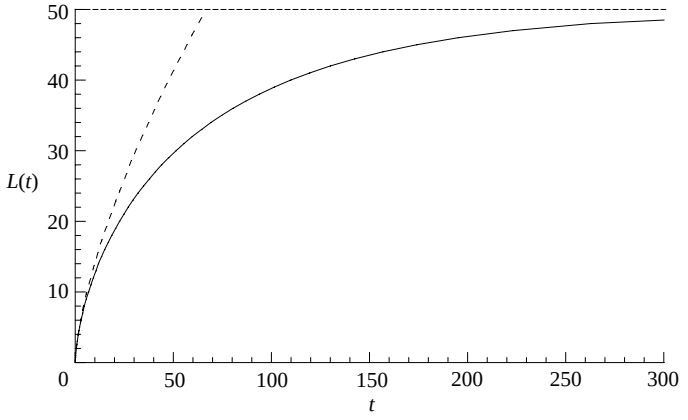

FIGURE 10. The dimensionless length of the intrusion, $L(t)$, as a function time for $E_1 = E_2 = C_{D1} = C_{D2} = 10^{-2}$ (——). The maximum length of this intrusion is 50. Also plotted is the dimensionless length as a function of time in the absence of entrainment, $E_1 = E_2 = 0$, and $C_{D1} = 10^{-2}$ (– – –).

(3.21), while the reduced equations governing the horizontal momentum are given by

$$\frac{\partial h_1}{\partial x} = \frac{C_{D1}(u_2 - u_1)|u_2 - u_1|}{h_1}, \tag{4.7}$$

$$C_{D2}(u_2 - u_1)|u_2 - u_1| = C_{D1}(u_3 - u_2)|u_3 - u_2|. \tag{4.8}$$

This corresponds to a balance between the streamwise pressure gradient and the interfacial drag for the lower layer, while for the intermediate layer the drag forces at the two interfaces balance each other. We further assume that the current has been sufficiently slowed so that $\mathscr{U} \gg |u_1|$ and thus

$$u_2 = \frac{\mathscr{U}}{1 + \Lambda}, \tag{4.9}$$

where $\Lambda = (C_{D1}/C_{D2})^{1/2}$. Thus we may integrate the governing equations to find

$$h_1 = \left[2C_{D1}u_2^2(L(t) + x)\right]^{1/2}, \qquad u_1 = -\frac{\mathrm{d}L}{\mathrm{d}t} - \frac{E_1}{(2C_{D1})^{1/2}}(L(t) + x)^{1/2} \tag{4.10}$$

where $x = -L(t)$ denotes the upstream length of the current. Then using the source condition that $u_1 h_1 = -1$ at $x = 0$, we find that $L(t)$ is given implicitly by

$$t + \frac{2(2C_{D1}L(t))^{1/2}}{E_1} - \frac{2}{E_1}\left(\frac{2C_{D1}}{E_1 u_2}\right)^{1/2} \tanh^{-1}\left[(E_1 u_2 L(t))^{1/2}\right] = 0. \tag{4.11}$$

An example of this solution is plotted in figure 10. The height of the mixed layer is given by

$$h_2 = (E_1 + E_2\Lambda)(x + L(t_0)), \tag{4.12}$$

where

$$x + L(t_0) = u_2(t - t_0). \tag{4.13}$$

In figure 11, we plot examples of these solutions when $E_1 = E_2 = 10^{-2}$, $C_{D1} = C_{D2} = 10^{-2}$ and $\mathscr{U} = 4$. The figure shows the height of the flow at various times as well as the steady state in which the front of the intruding layer has been arrested.

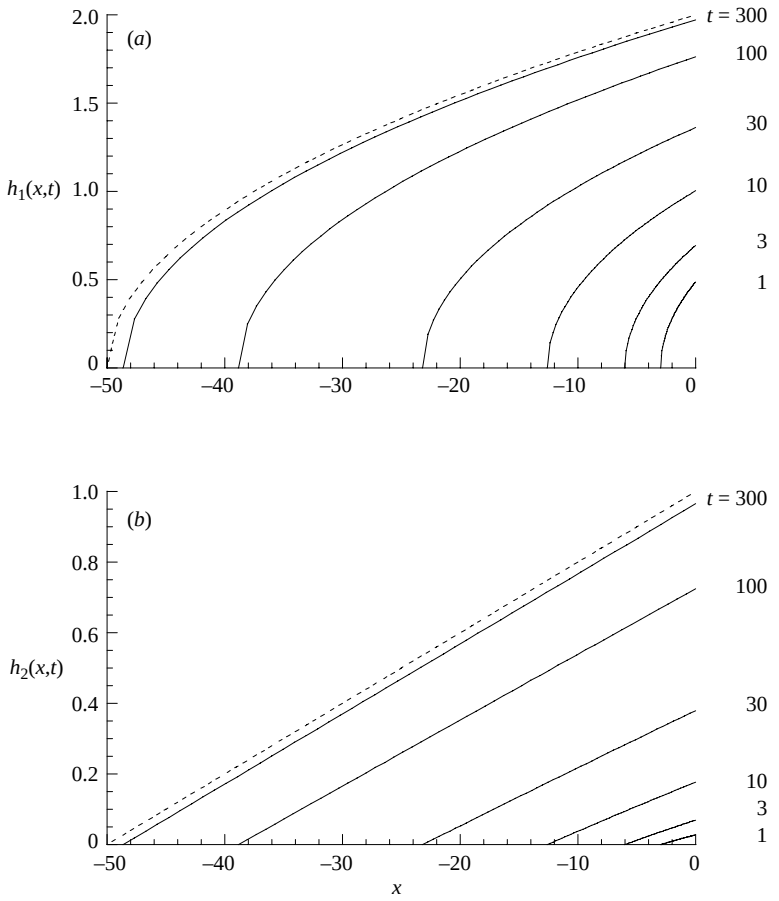

FIGURE 11. The height profiles of (*a*) the lower layer and (*b*) the mixed layer as function of distance at times $t = 1, 3, 10, 30, 100, 300$ for $E_1 = E_2 = C_{D1} = C_{D2} = 10^{-2}$. Also plotted are the steady profiles (– – –).

There are several noteworthy features of the solutions. First the height of the lower layer decreases towards the front of the current so that the streamwise pressure gradient may balance the interfacial drag. This nose-down characteristic has been observed in other studies of gravity currents propagating against some form of resistance (see, for example, Hogg, Ungarish & Huppert 2000; Hogg & Woods 2001). In the absence of entrainment between the intermediate and lower layer ($E_1 = 0$), the length is given by

$$L(t) = \left(\frac{9}{8C_{D1}}\right)^{1/3} t^{2/3}. \tag{4.14}$$

Thus the drag has slowed the motion from its initial constant speed, but it does not lead to the arrest of the layer, because fluid is being continually added to it. However if $E_1 > 0$ then the maximum length attained is $(E_1 u_2)^{-1}$; fluid is now lost by mixing into the overlying layer and the velocity and height fields evolve towards a steady state.

Stationary salt wedges have been traditionally modelled as two-layer systems in which the pressure gradient associated with the basal saline layer is balanced by interfacial drag associated with the over-riding mean flow (see, for example, Schijf &

Schönfeld 1953). Such models do not include a mixed layer and do not account for mixing between the saline and fresh fluids. Therefore if the salt wedge is stationary, the lower layer must carry zero volume flux ($q=0$) because, as illustrated by the preceding solution, without mixing across the interface there is no way of forming a steady state. There are no such limitations in terms of our new model presented above.

We now calculate the steady, three-layer model of an arrested salt wedge by integration of the steady governing equations from the point at which the height and velocity of the lower layer vanish; this corresponds to the foremost point of the arrested wedge. It is a singular point of the governing equations. Thus to construct the solution we must determine a series expansion away from this point. For notational convenience we locate the foremost point at $x=0$ and formulate series expansion for the height, velocity and reduced gravity of each layer in $0<x\ll 1$. We find that the height fields are given by

$$h_1=\left(1-\frac{\mathscr{U}^2}{\mathscr{H}}\right)^{-1/2}\frac{\mathscr{U}\sqrt{2C_{D1}}}{1+\Lambda}x^{1/2}+\ldots,\quad h_2=(E_1+E_2\Lambda)x+\ldots,\quad h_3=\mathscr{H}+\ldots. \tag{4.15}$$

The velocity of each layer is given by

$$u_1=-\frac{E_1}{\sqrt{2C_{D1}}}\left(1-\frac{\mathscr{U}^2}{\mathscr{H}}\right)^{1/2}x^{1/2}+\ldots,\quad u_2=\frac{\mathscr{U}}{1+\Lambda}+\ldots,\quad u_3=\mathscr{U}+\ldots. \tag{4.16}$$

Finally, the reduced gravities of the lower and intermediate layers and the surface pressure are given by

$$g_1'=1\quad g_2=\frac{E_2}{E_1+E_2\Lambda}+\ldots,\quad p_0=\frac{-U^3\sqrt{2C_{D1}}}{\mathscr{H}(1+\Lambda)}\left(1-\frac{\mathscr{U}^2}{\mathscr{H}}\right)^{-1/2}x^{1/2}+\ldots \tag{4.17}$$

Using these series expansions we may integrate the governing equations numerically until either we find a position at which the volume flux in the lower layer is equal to unity ($u_1h_1=-1$), or until we reach a point of hydraulic control. In multi-layer flows, these correspond to a position at which the speed of one of the internal, small-amplitude waves becomes stationary (Baines 1988; Lane-Serff 1993). For this three-layer motion this occurs when

$$\Gamma=h_1h_2h_3g_1'g_2'\left[F_3^2F_2^2+\lambda F_3^2-\lambda^2+\left(F_1^2-1\right)\left(F_2^2+F_3^2-\lambda\right)\right]=0, \tag{4.18}$$

where $F_i^2=u_i^2/[g_1'h_i]$ and $\lambda=g_2'/g_1'$. We note that in the absence of an intermediate mixed layer ($F_2^2\to\infty$), this expression reduces to $F_3^2+F_1^2=1$, which is the critical composite Froude number for Boussinesq two-layer flows introduced by Armi & Farmer (1986).

In figure 12 we plot some example solutions for which $E_1=E_2=10^{-2}$, $C_{D1}=C_{D2}=10^{-2}$, $\mathscr{U}=4$ and $\mathscr{H}$ varies between 30.42 and 200. When $\mathscr{H}=30.42$ we find that hydraulic control is attained ($\Gamma=0$) when $u_1h_1=-1$. When $\mathscr{H}$ exceeds this value the flux attains -1 before the point of hydraulic control $\Gamma<0$. We note that the velocity and reduced gravity of the intermediate layer (u_2 and g_2') and are approximately constant for these parameters and that the solution of the reduced system of equations presented above provides a reasonably good representation of the dynamics. As with the classical model of a saline wedge, we note that the gradient of the interfacial height has singular points both at the foremost edge of the intrusion and at the point of hydraulic control.

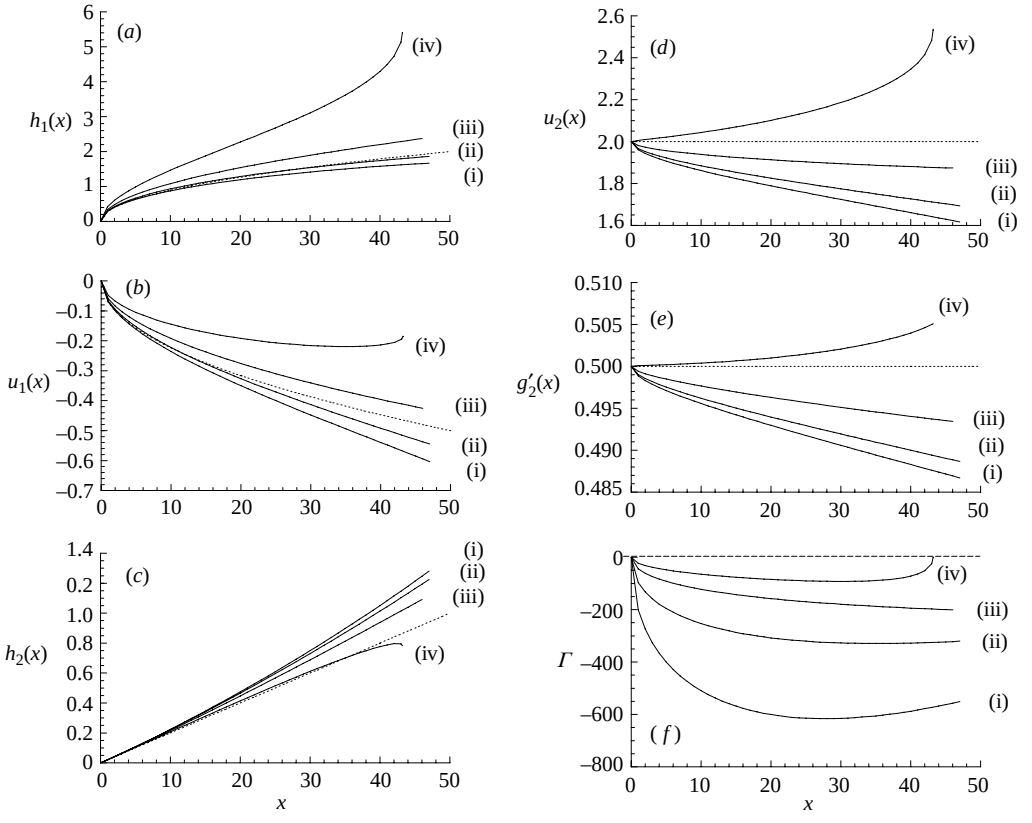

FIGURE 12. The height and velocity of the lower layer, h_1 and u_1 (a, b), the height, velocity and reduced gravity of the mixed layer, h_2, u_2, g_2' and Γ $(c–f)$ as functions of distance from the foremost point. Curve (i) $\mathscr{H} = 200$; (ii) $\mathscr{H} = 100$; (iii) $\mathscr{H} = 50$; and (iv) $\mathscr{H} = 30.42$. The dashed line denotes the theory for a deep ambient.

5. Particle-driven currents

When the density of the intruding fluid is due to the presence of suspended heavy particles, the motion shares many features with the compositional currents described in the previous section. However, and most importantly, particle settling progressively reduces the buoyancy of the flow and consequently reduces the velocity of the gravity current. For these flows, driven by a constant flux of dense fluid, a steady state may be attained in which the spatial gradient of the horizontal flux of particulate is balanced by settling out of the flow to the underlying boundary (see Bonnecaze *et al.* 1995; Hogg & Woods 2001). As will be shown below, this is an important feature of these flows because they evolve towards a state in which the volume fraction of particles decays exponentially with distance from the source. In dimensional terms the horizontal lengthscale over which settling occurs is q/v_s, while the timescale for this process is $q(g_0'q)^{-1/3}/v_s$ (Hogg *et al.* 2000).

In this section we first consider single-layer models of the motion. We compute numerical solutions to the governing equations, derive a simplified 'integral' model of the flow and compare both models with the experimental observations. Thereafter we analyse the longer term motion and demonstrate how the intrusion may be arrested

by interfacial drag forces to adopt a wedge-like profile which is analogous to the saline wedges of § 4.

5.1. *Single-layer models*

When the depth of the particle-laden fluid is sufficiently shallow relative to the depth of the ambient, and interfacial drag and mixing between the intruding and ambient fluid may be neglected, the dimensionless governing equations for the flow are considerably simpler than the full system presented in § 3. The motion may then be studied by modelling only the lower layer. In terms of the rescaled spatial and temporal variables, $X = \mathscr{V}_s x$ and $T = \mathscr{V}_s t$, the equations that represent conservation of mass and momentum and the transport of suspended particulate are

$$\frac{\partial h_1}{\partial T} + \frac{\partial}{\partial X}(u_1 h_1) = 0, \tag{5.1}$$

$$\frac{\partial}{\partial T}(u_1 h_1) + \frac{\partial}{\partial X}\left(u_1^2 h_1 + \tfrac{1}{2} g_1' h_1^2\right) = 0, \tag{5.2}$$

$$\frac{\partial}{\partial T}(h_1 g_1') + \frac{\partial}{\partial X}(u_1 h_1 g_1') = = -g_1'. \tag{5.3}$$

Note that the dimensionless reduced gravity is equivalent to the volume fraction of suspended particles normalized by its initial value. The conditions at the source are

$$g_1' = 1, \qquad u_1 h_1 = 1/2. \tag{5.4}$$

A further condition specifying the Froude number at the source may be enforced only if the flow is supercritical; otherwise the Froude number is determined by the interior motion. At the front of the flow, $X = X_N(t)$, we impose the condition

$$u = \mathscr{U} + Fr(g_1' h_1)^{1/2}, \tag{5.5}$$

where we have established empirically that $Fr = 0.81$. We may also calculate the dimensionless rate of deposition, defined by

$$\eta(X) = \frac{1}{D}\int_{T_s}^{D} g_1' \, \mathrm{d}T, \tag{5.6}$$

where $X_N(T_s) = X$ and D denotes the dimensionless duration of the experiment. We note that the distribution of the deposited particles for flows of relatively long duration ($D \gg 1$) is identical to the distribution of suspended sediment.

We numerically integrate these equations using an explicit two-step Lax–Wendroff scheme, having first reformulated the governing equations in terms of a rescaled spatial variable $\xi = X/X_N$, so that $0 \leqslant \xi \leqslant 1$. Boundary conditions are enforced by calculation of the dependent variables along characteristics that point out of the domain. This method is described in detail in Bonnecaze *et al.* (1993); for the flows under consideration in this study, the boundary conditions at the source are different but are readily imposed. It is necessary to add a minimal amount of artificial viscosity to maintain numerical stability.

We first consider the motion in an otherwise quiescent ambient fluid $\mathscr{U} = 0$. Profiles of the height, velocity and reduced gravity at various times for a subcritical source are plotted in figure 13. We note that after a sufficient period, critical conditions are established at the source and the profiles begin to adopt a steady distribution. Furthermore, we find that the volume fraction of particles in the current decays approximately exponentially with distance from the source ($g_1' \sim \exp(-2X)$) and that the rate of deposition, η, also approaches this distribution. The origin of this exponential

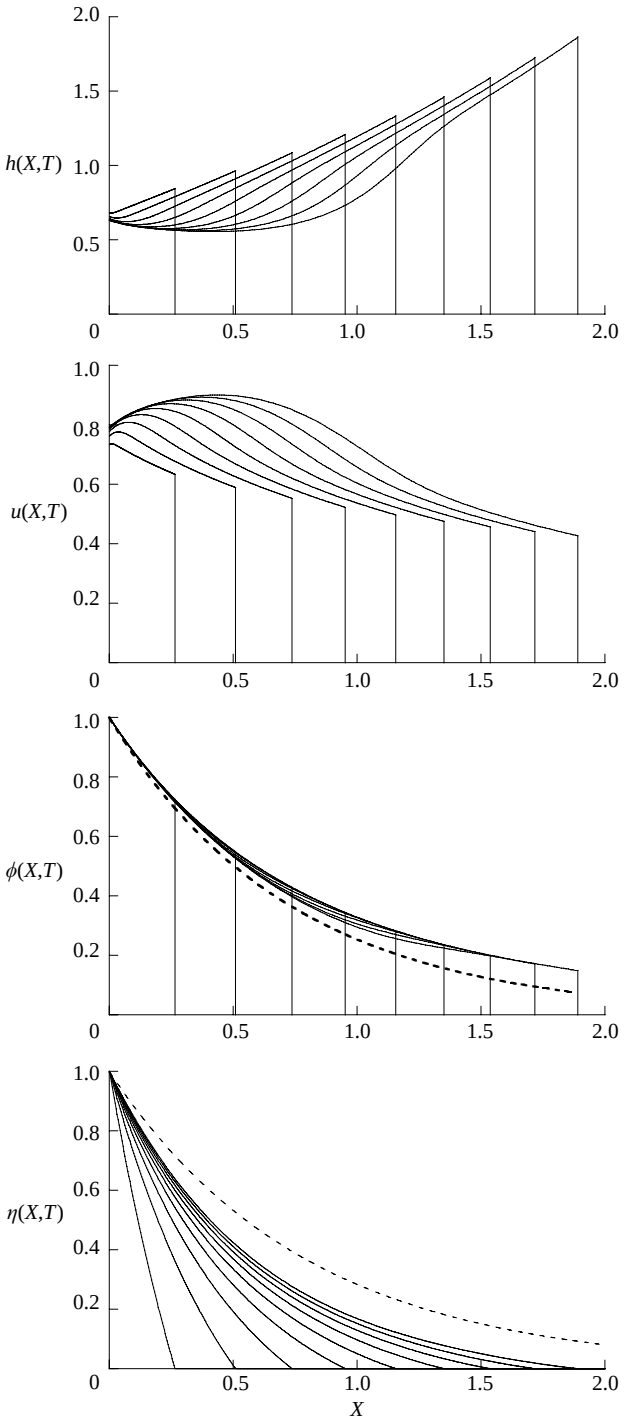

FIGURE 13. The height, $h(X, T)$, velocity, $u(X, T)$, volume fraction of particles, $\phi(X, T)$, deposit, $\eta(X, T)$ of a particle-driven gravity current as a function of the rescaled distance X in the absence of an ambient flow at rescaled times $T = 0.4, 0.8, 1.2, 1.6, 2.0, 2.4, 2.8, 3.2, 3.6$. Also plotted is the steady distribution of the volume fraction of particles, $\phi = \exp(-2X)$ (– – –).

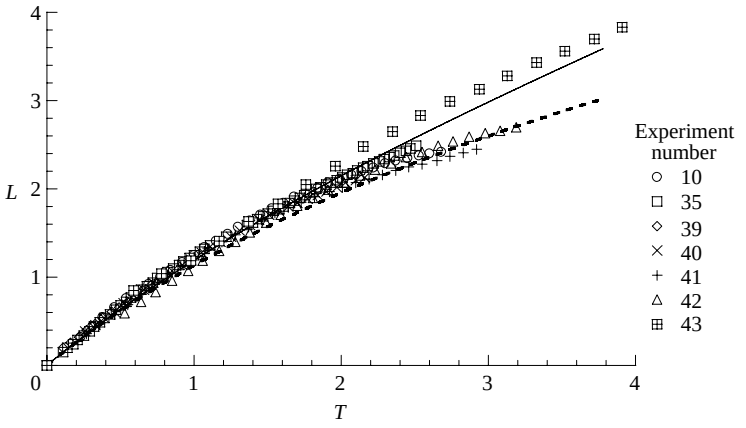

FIGURE 14. The rescaled length of the particle-driven gravity currents, L, as a function of rescaled time, T, for all of the experimental data series in the absence of a mean ambient flow. The theoretical curves are the single-layer shallow-water equations (——) and the integral model (– – –).

distribution may be readily understood. It emerges from the steady balance between the divergence of the horizontal flux of particles and the settling flux to the underlying boundary ($\partial(u_1 h_1 g_1')/\partial X \sim -g_1'$)

We find that the speed of the flow and the distribution of the deposit may be reasonably accurately modelled using a simplified 'integral' model, akin to the 'box' models for instantaneous releases of particle-laden flow (Dade & Huppert 1994; Hallworth *et al.* 1998; Harris *et al.* 2001). This model is formulated in terms of the height, volume and position of the front, denoted by h_N, ϕ_N and X_N, respectively. The volume flux at the front is then equated with the volume flux at the source

$$h_N \frac{\mathrm{d}X_N}{\mathrm{d}T} = \frac{1}{2}, \tag{5.7}$$

and the Froude number condition is given by

$$\frac{\mathrm{d}X_N}{\mathrm{d}T} = Fr(\phi_N h_N)^{1/2}. \tag{5.8}$$

Finally, the sedimentation of particles from the front is given by

$$\frac{\mathrm{d}\phi_N}{\mathrm{d}T} = -\frac{\phi_N}{h_N}. \tag{5.9}$$

These equation may be integrated to yield $\phi_N = \exp(-2X_N)$ and

$$X_N = \frac{3}{2}\log\left(1 + \frac{(2Fr)^{2/3}T}{3}\right). \tag{5.10}$$

Then, on the further assumption that behind the front of the current, the volume fraction of particles has adopted a steady, exponentially decaying profile, we find that

$$\eta(X) = \exp(-2X)\left[1 - \frac{t_s}{D}\right]_+, \tag{5.11}$$

where $X_N(t_s) = X$ and $[\ldots]_+$ denotes the Heaviside step function.

We compare the theoretical predictions for the length of the current as a function of time, ($L = 2X_N(T)$), with the experimental observations in figure 14. We note

that adopting the new rescaled dimensionless variables has, with the exception of one set of experimental conditions, collapsed the data onto a single curve and that even the exceptional experiment is not far from the same curve. Furthermore there is good agreement between the experimental results and the predictions of both the shallow-water and integral models. The shallow-water model and the integral model only begin to diverge from each other at late stages of the flow. (We find that the calculated positions of the front are within 6 % of each other when over 95 % of the particles have settled out of the flow.) The data series that does not fit well with this model (Experiment 43) was conducted using particles of diameter 53 μm. These have the largest settling velocity of all those used in this study and have the greatest tendency to be stratified within the reservoir used to deliver the particles to the flume. Thus it may be that the volume fraction of suspended sediment was not constant throughout the experiment.

We also compare in figure 15 the measured distributions of the deposited particles with the predictions of the integral model. (There are negligible differences between the predictions of the integral and shallow-water models of this quantity.) We observe that apart from directly under the source, where the impingement of the plume delivering the particle-laden fluid upon the underlying boundary inhibits deposition, there is good agreement between the theoretical predictions and experimental observations.

We numerically integrate the single-layer model of the gravity current motion to elucidate the effects of an ambient flow. The magnitude of the mean flow compared to the buoyancy velocity scale ($\mathscr{U} > 0$) is an important new parameter and along with the Froude number, Fr, are the only remaining dimensionless groups in the governing equations after adopting the rescaled spatial and temporal scales, X and T. Our experiments correspond to different values of $\mathscr{U}$ in the range 0.59 to 1.2, although the initial conditions for each run were chosen such that there were essentially four different values of $\mathscr{U}$, namely 0.59, 0.75, 0.94 and 1.2. The experimental data and the numerically calculated position of the upstream and downstream fronts of the current are plotted in figure 16. Again it is evident that for each value of $\mathscr{U}$ the rescaled variables collapse the data onto single curves. Furthermore there is good agreement between the experimental observations and the theoretical predictions.

Also plotted in figure 16 are the results from an 'integral' model of the flow. The flux of fluid and the evolution of the volume fraction of particles at the front are still given by (5.7) and (5.9), but the Froude number condition at the front is now given by

$$\frac{\mathrm{d}X_N}{\mathrm{d}T} = \mathscr{U} + Fr(\phi_N h_N)^{1/2}. \tag{5.12}$$

Integrating this system of ordinary differential equations provides a prediction for the speed of the upstream and downstream fronts that agrees well with the experimental data (figure 16). The integral and shallow-water models diverge at late times, but by this stage the volume fraction of particulate is considerably reduced from its initial value and so the current is transporting very little sediment.

Finally we calculate the distribution of the rate of deposition, $\eta(X)$, using the integral model (although we note that the predictions from the shallow-water model are very similar). We plot the experimental data and theoretical predictions in figure 17 and note that there is reasonable agreement between the two. The largest differences occur for flows driven by the smallest volume flux of fluid ($q \approx 25\,\mathrm{cm^2\,s^{-1}}$: Experiments 13, 30, 34). These flows may have begun to be influenced by drag forces, which have been neglected in these calculations.

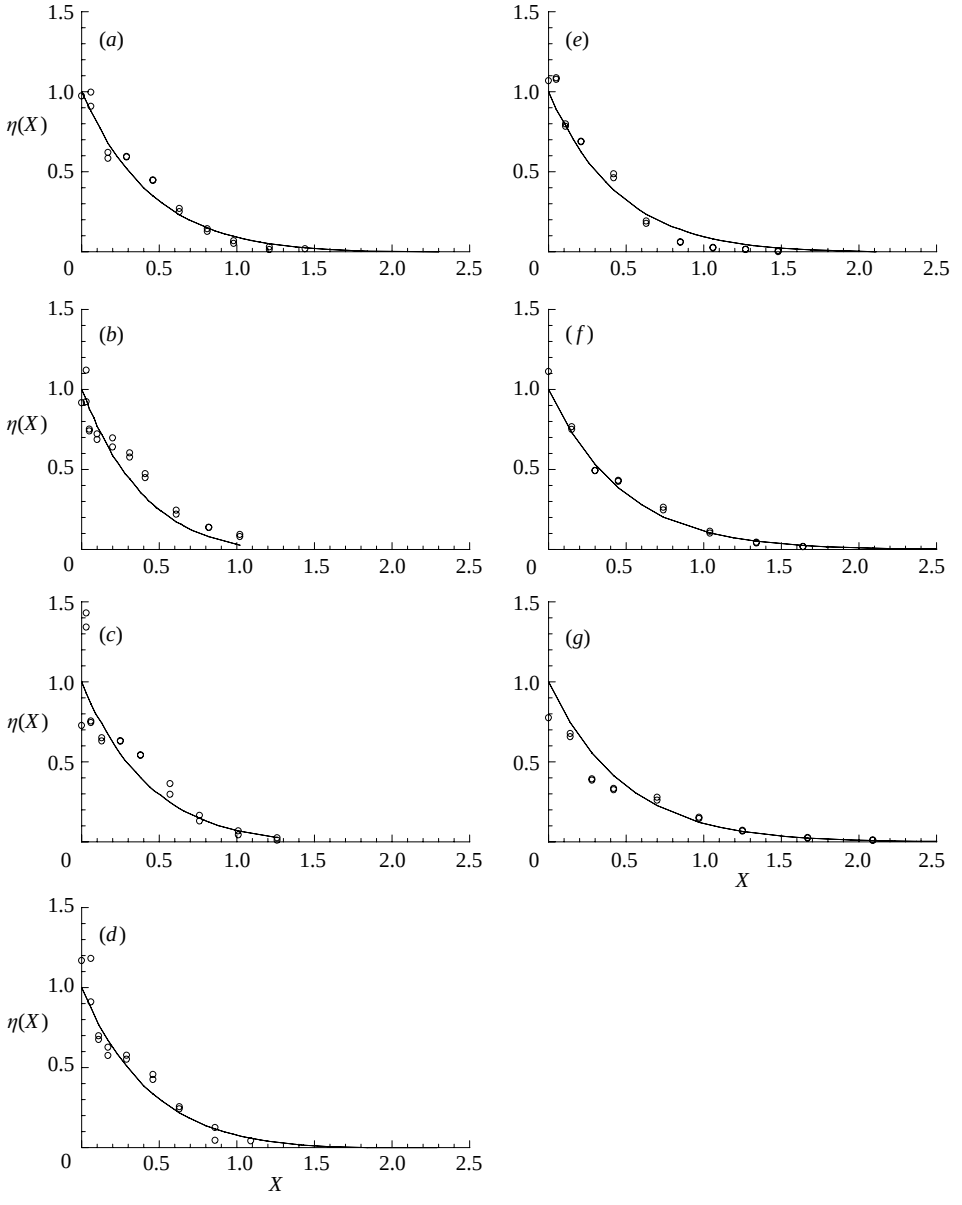

FIGURE 15. The distribution of the rate of deposition, $\eta(X)$, as a function of rescaled distance after the flow has finished, plotting experimental data (○) and theory (——) for (*a*) Experiment 10 ($D = 6.28$); (*b*) Experiment 35 ($D = 2.65$); (*c*) Experiment 39 ($D = 4.38$); (*d*) Experiment 40 ($D = 4.84$); (*e*) Experiment 41 ($D = 6.81$); (*f*) Experiment 42 ($D = 13.47$); and (*g*) Experiment 43 ($D = 14.54$).

5.2. *The effects of drag*

Although we have demonstrated that these experiments were largely unaffected by interfacial drag forces, at least during their initial phases, larger scale flows may be strongly resisted by the motion of the ambient. In this subsection we analyse the dynamics of a particle-laden intrusion that is arrested to form a steady, wedge-like

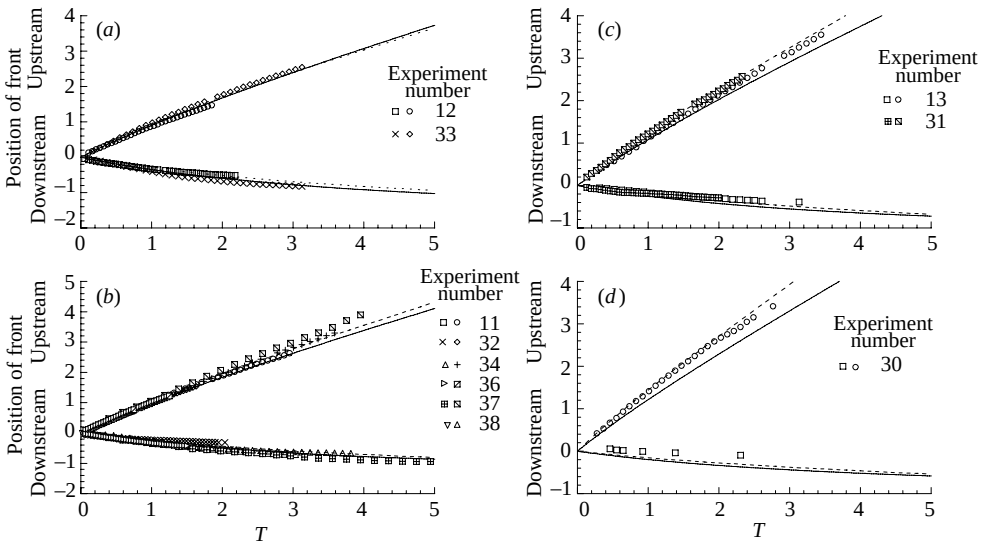

FIGURE 16. The position of the upstream and downstream fronts of a particle-driven gravity current propagating in the presence of a mean flow as function of time for (*a*) $\mathscr{U} = 0.59$, (*b*) $\mathscr{U} = 0.75$, (*c*) $\mathscr{U} = 0.94$ and (*d*) $\mathscr{U} = 1.2$. Predictions of single-layer shallow-water theory (——) and the integral model (– – –) are also plotted.

layer. This is similar to the saline wedge studied in § 4.2, but in this case the excess density is due solely to the presence of suspended particles. There are important differences between the saline and particle-laden situations that are revealed by this analysis. Perhaps most importantly is that in contrast to the compositionally driven flows, it is not possible to have a stationary lower layer because settling continually reduces the volume fraction of particles in suspension. Rather, in the steady state the losses due to sedimentation must be balanced by horizontal transport by the flow. It is also not possible to use a steady, single-layer model by simply incorporating an interfacial drag term in the momentum equation (5.2). Such a model, irrespective of source conditions, evolves towards an interior point at which the flow becomes critical ($u_1^2 = g_1' h_1$) and thereafter only unsteady evolution is possible.

We employ the formulation of § 3 to establish the steady profiles of the height, velocity and reduced gravity of the lower dense layer, the intermediate mixed layer and the overlying ambient layer. We account for drag and mixing between the layers and find that as with the compositionally driven flow, mixing is necessary to establish a steady, arrested state. However, particle settling introduces some important differences because the reduced gravity of the lower layer now varies spatially and, as is shown below, vanishes at the front of the current. We seek steady solutions to (3.18)–(3.26) such that the volume flux of the lower layers vanishes at the front, which we locate at $x = 0$. The equations are singular at this point, but we may construct series expansions for $x \ll 1$ so that the equations may be integrated away from the origin.

First the dominant balance of forces in the momentum equation of the mixed layer is between the drag forces. Thus we find that

$$u_2 = \frac{u_3}{1 + \Lambda} + \ldots \qquad \text{for} \qquad x \ll 1. \tag{5.13}$$

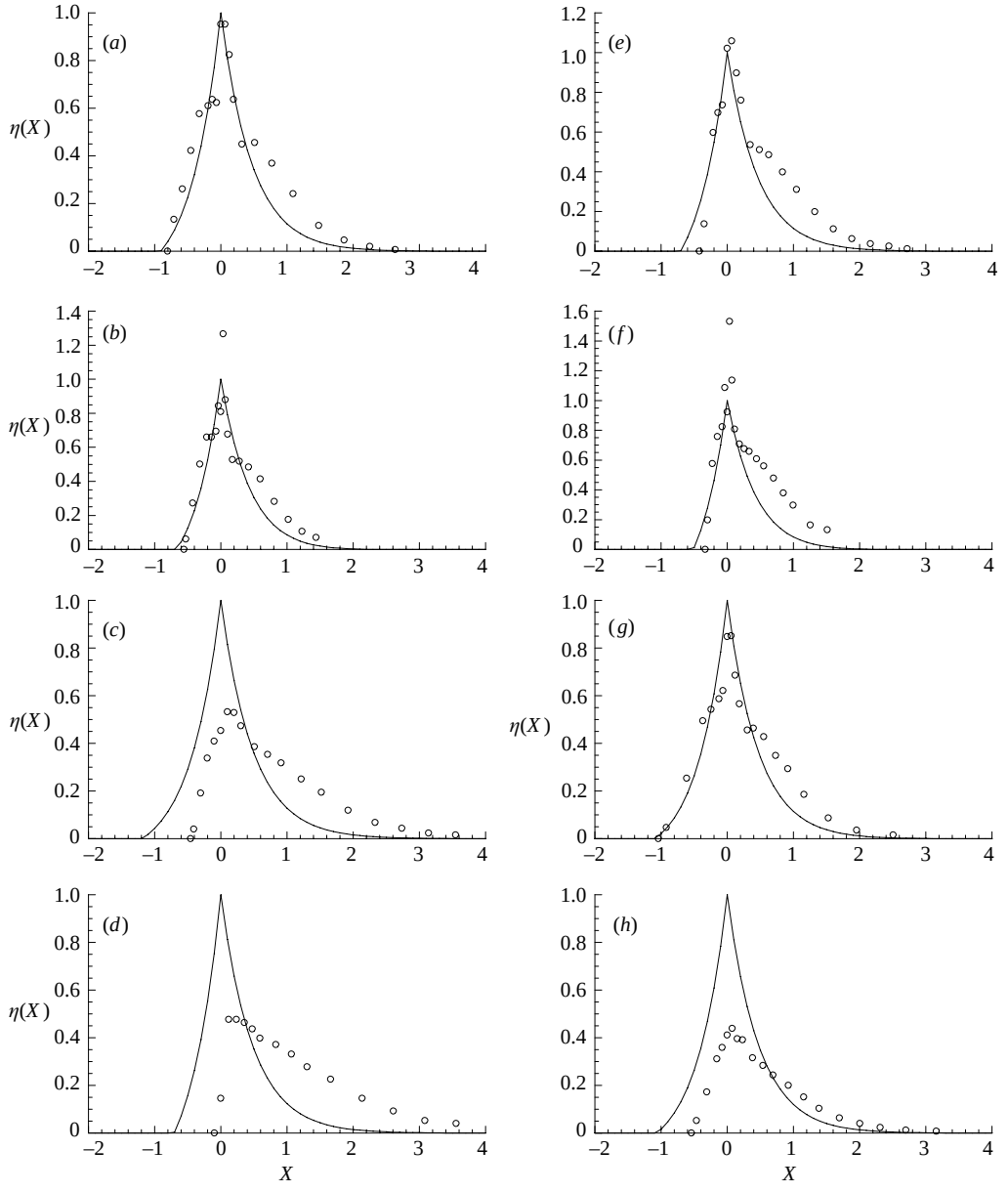

FIGURE 17(*a–h*). For caption see facing page.

The volume fluxes of fluid are then given by

$$u_1h_1 = -\frac{E_1u_3x}{1+\Lambda} + \ldots, \qquad u_2h_2 = \frac{(E_1+E_2\Lambda)u_3x}{1+\Lambda} + \ldots, \qquad u_3h_3 = \mathscr{H}\mathscr{U} + \ldots. \tag{5.14}$$

This implies that the reduced gravities of the lower two layers take the form

$$g_1' = Ax^\alpha + \ldots, \qquad g_2' = ABx^\alpha + \ldots, \tag{5.15}$$

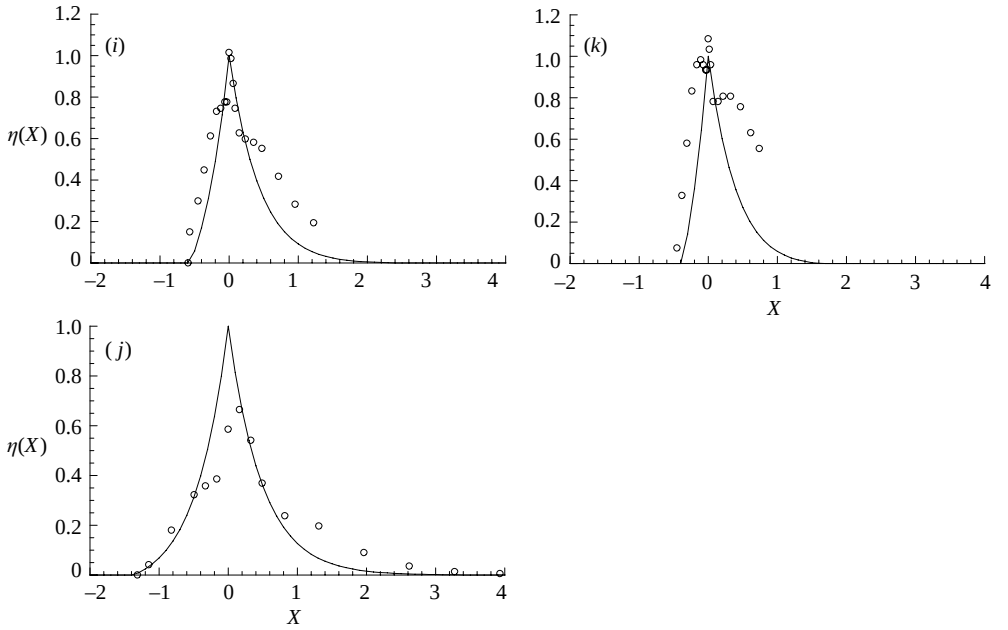

FIGURE 17. The distribution of the rate of deposition, $\eta(X)$, as a function of rescaled distance after the flow has finished, plotting experimental data (○) and theory (——) for (*a*) Experiment 11 ($D=6.21$, $\mathscr{U}=0.75$); (*b*) Experiment 12 ($D=2.86$, $\mathscr{U}=0.59$); (*c*) Experiment 13 ($D=15.26$, $\mathscr{U}=0.94$); (*d*) Experiment 30 ($D=7.74$, $\mathscr{U}=1.2$); (*e*) Experiment 31 ($D=5.38$, $\mathscr{U}=0.94$); (*f*) Experiment 32 ($D=2.44$, $\mathscr{U}=0.74$); (*g*) Experiment 33 ($D=6.81$, $\mathscr{U}=0.60$); (*h*) Experiment 34 ($D=8.22$, $\mathscr{U}=0.73$); (*i*) Experiment 36 ($D=2.84$, $\mathscr{U}=0.75$); (*j*) Experiment 37 ($D=15.35$, $\mathscr{U}=0.75$); and (*k*) Experiment 38 ($D=1.64$, $\mathscr{U}=0.74$).

where A is an as yet undetermined constant and α and B satisfy

$$\alpha = \frac{\mathscr{V}_s(1+\Lambda)}{E_1 u_3}(1-B), \tag{5.16}$$

$$\alpha B = -B\left(\frac{\mathscr{V}_s(1+\Lambda)}{(E_1+E_2\Lambda)u_3}+1\right)+\frac{E_1}{E_1+E_2\Lambda}. \tag{5.17}$$

These yield two values for α; for these flows the reduced gravity must remain finite and so $\alpha>0$. Thus the reduced gravity of both layers vanishes at the front of the intrusion. This means that the buoyancy-induced pressure gradient in the lower layer cannot balance the interfacial drag at the front and the balance of forces at the front is different from that of the compositionally driven intrusion. Given (5.15) it implies that the heights of the layers are given by

$$h_1 = h_0+\ldots, \qquad h_2=(E_1+E_2\Lambda)x+\ldots, \qquad h_3=\mathscr{H}-h_0+\ldots, \tag{5.18}$$

where h_0 is a constant. Finally we deduce that

$$u_1=-\frac{E_1u_3x}{(1+\Lambda)h_0}+\ldots \qquad u_3=\frac{\overline{u}}{1-h_0/\mathscr{H}}+\ldots, \qquad p_0=-\frac{h_0A}{2}x^{\alpha}+\ldots. \tag{5.19}$$

Using these series we may then integrate numerically until critical conditions ($\Gamma=0$) are attained (see § 4.2). We plot some illustrative profiles in figure 18.

The form of the solution near the front with $g_1', g_2' \to 0$ as $x\to 0$ arises due to the model of particle transport in this study. As explained in § 3, the suspension is assumed

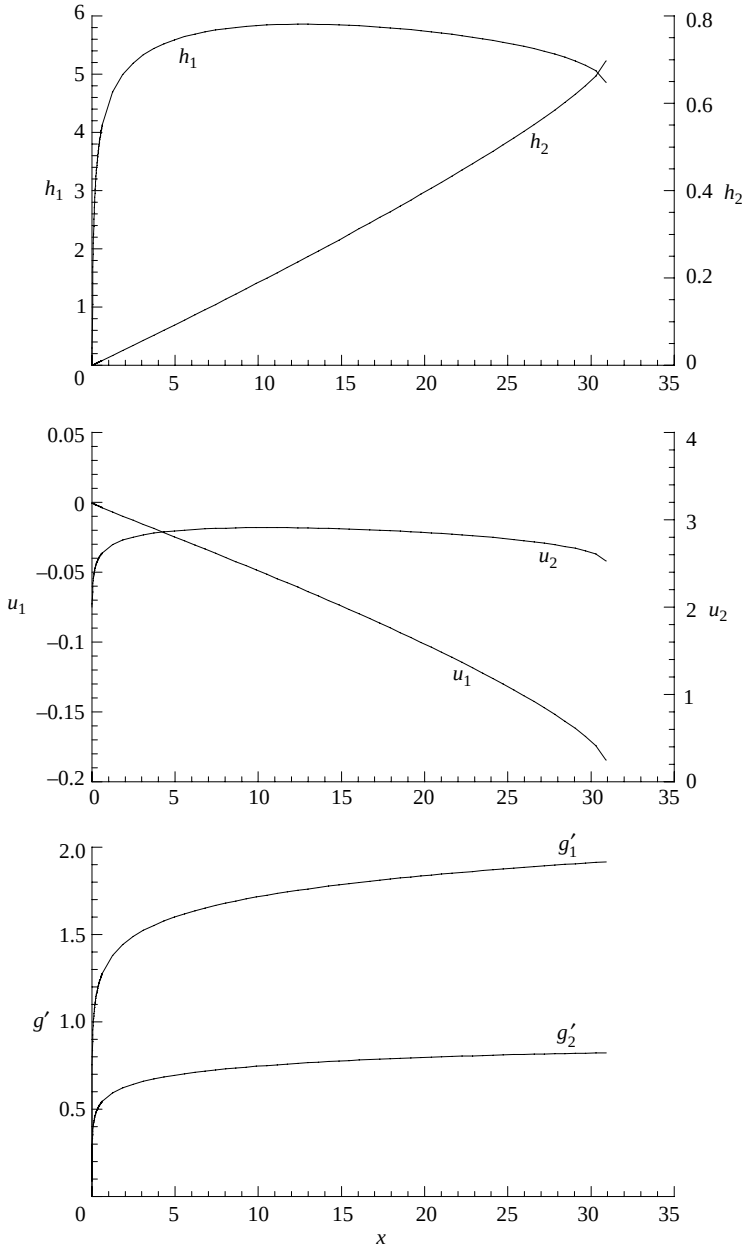

FIGURE 18. The heights, $h_1(x), h_2(x)$, velocities, $u_1(x), u_2(x)$, reduced gravities, $g'_1(x), g'_2(x)$ of the lower and intermediate mixed layers as function of distance from the foremost point. Parameter values are $\mathscr{H} = 20$, $E_1 = E_2 = 10^{-2}$, $C_{D1} = C_{D2} = 10^{-2}$, $\mathscr{U} = 4$, $h_0 = 0.1$ and $\mathscr{V}_s = 5 \times 10^{-3}$.

to be vertically well-mixed by the fluid turbulence with sedimentation occurring through a lower viscous layer. For constant-flux currents this leads to the volume fraction decaying exponentially with distance, which appears to be consistent with the experimental observations. However when the flow has slowed sufficiently it is unlikely to generate sufficient turbulence to suspend the particles and thus this model of the

particles being well-mixed throughout the fluid layer may no longer be appropriate. In such circumstances it may be more appropriate to demarcate the boundary between the layers as a kinematic settling front. Such a model has been formulated in the context of gravity current motion by Ungarish & Huppert (1998). Then the reduced gravity of the layer is not reduced by settling, because the volume fraction of particles is maintained; rather the height of the layer is reduced by the sedimentation process. A change of this nature strongly affects the structure of the solution close to the arrested front. The reduced gravity of the layers would not vanish and the dominant forces in the lower layer could be between the drag and the buoyancy-induced pressure gradient. The representation of this change in the settling behaviour within a depth-averaged model remains an interesting and potentially important outstanding issue for future study of these flows.

6. Summary and conclusions

Although high-Reynolds-number gravity currents generated in the laboratory from sustained sources of saline or particle-laden fluid are turbulent and exhibit complicated, fluctuating flow structures, we have demonstrated that the initial motion in the presence of a mean flow is primarily determined by the relative magnitudes of three velocity scales. In dimensional form, these are the mean flow speed, $\overline{u}$, the buoyancy-induced velocity, $(g_0' q)^{1/3}$, and the settling velocity of the constituent particles, v_s. Compositionally driven flows propagate at a constant speed, whereas because particle sedimentation progressively reduces the bulk density, particle-driven flows decelerate. The two effects of buoyancy-driven motion and the mean flow are essentially additive: downstream flow speeds are supplemented by the mean flow, whereas upstream flow speeds are reduced.

In this contribution we have quantified experimentally the effects of the ambient flow upon the density-driven motion and, for particle-laden fluid, we have determined the distribution of the deposited particles during the entire flow. We found that considerable practical measures were required to ensure that a homogeneous suspension was delivered at a constant rate. We have also made several theoretical advances by identifying the key dimensionless ratios that specify the dynamical regime of these flows and by formulating shallow-layer and integral models of the motion. We demonstrated that the predictions of both models are in close agreement with the experimental observations.

After sufficiently long times and at sufficient distances from the source, the flow becomes influenced by additional flow processes. These include drag and mixing between the fluid layers. Even though our experiments were conducted in a relatively long flume, these effects remained negligible within the regime we considered. Nevertheless we have formulated a multi-layered mathematical model of the motion that may be used at long times. For upstream flows in particular, we have demonstrated that it is crucial to capture the exchange between layers if an arrested flow state, such as an estuarine wedge, is to be resolved accurately. Our illustrative calculations are based upon the simple models of the complex, interfacial flow processes; however the same analytical framework may be readily employed with different closure assumptions.

Our study, which we believe provides the first investigation of how sustained particulate gravity currents interact with a mean flow, has many applications. Examples include the dispersion of solid pollutants within an estuary, which is governed by a competition between density-driven dispersal and advection by the background flow, and the formation of sediment deposits within the deep ocean by turbidity flows, which

interact with a mean current. There are number of features of this type of motion that warrant further investigation. For instance how is the propagation modified if the dense fluid is introduced from a localized source and allowed to spread laterally as well as up- and downstream? What controls the interfacial drag and mixing processes and how may they be modelled mathematically? And finally, how may these results be applied to models of the wind-driven dispersion of plumes of volcanic ash?

REFERENCES

Altinakar, M. S., Graf, W. H. & Hopfinger, E. J. 1996 Flow structure in turbidity currents. *J. Hydr. Res.* **34**, 713–718.

Anati, D. A., Assaf, G. & Thompson, R. O. R. Y. 1977 Laboratory models of seas straits. *J. Fluid Mech.* **81**, 341–351.

Arita, M. & Jirka, G. H. 1987*a* Two-layer model of saline wedge i: entrainment and interfacial friction. *J. Hydr. Engng* **113**, 1229–1247.

Arita, M. & Jirka, G. H. 1987*b* Two-layer model of saline wedge ii: prediction of mean properties. *J. Hydr. Engng* **113**, 1249–1263.

Armi, L. & Farmer, D. M. 1986 Maximal two-layer exchange through a contraction with barotropic net flow. *J. Fluid Mech.* **164**, 27–51.

Baines, P. G. 1988 A general method for determining upstream effects in stratified flow of finite depth over long obstacles. *J. Fluid Mech.* **188**, 1–22.

Benjamin, T. B. 1968 Gravity currents and related phenomena. *J. Fluid Mech.* **31**, 209–248.

Benjamin, T. B. 1981 Steady flows drawn from a stably stratified reservoir. *J. Fluid Mech.* **106**, 245–260.

Bonnecaze, R. T., Hallworth, M. A., Huppert, H. E. & Lister, J. R. 1995 Axisymmetric particle-driven gravity currents. *J. Fluid Mech.* **294**, 93–121.

Bonnecaze, R. T., Huppert, H. E. & Lister, J. R. 1993 Particle-driven gravity currents. *J. Fluid Mech.* **250**, 339–369.

Buckee, C., Kneller, B. & Peakall, J. 2001 Turbulence strucutre in steady, solute-driven gravity currents. *Spec. Publ. Intl Assoc. Sediment.* **31**, 173–187.

Bühler, J., Wright, S. J. & Kim, Y. 1991 Gravity currents advancing into a co-flowing fluid. *J. Hydr. Res.* **29**, 243–257.

Bühler, J., Wright, S. J. & Kim, Y. 1992 Source control of intrusions along horizontal boundary. *J. Hydr. Engng* **29**, 442–459.

Cavalletti, A. & Davies, P. A. 2003 Impact of vertical turbulent, planar, negatively buoyant jet with rigid horizontal bottom boundary. *J. Hydr. Engng* **129**, 54–62.

Dade, W. B. & Huppert, H. E. 1994 Predicting the geometry of channelised deep-sea turbidites. *Geology* **22**, 9645–9648.

Dade, W. B. & Huppert, H. E. 1995 A box model for non-entraining suspension-driven gravity surges on horizontal surfaces. *Sedimentology* **42**, 453–471.

Dalziel, S. B. 1991 Two-layer hydraulics: a functional approach. *J. Fluid Mech.* **223**, 135–163.

Ellison, T. H. & Turner, J. S. 1959 Turbulent entrainment in stratified flows. *J. Fluid Mech.* **6**, 423–448.

Felix, M. 2002 Flow strucutre of turbidity currents. *Sedimentology* **49**, 397–419.

Gilmour, U. P. & Woods, A. W. 1994 Mixing experiments on fluid released near the closed end of a two-dimensional channel. *J. Hazard. Mat.* **36**, 227–247.

Gratton, J. & Vigo, C. 1994 Self-similar gravity currents with variable inflow revisited: plane currents. *J. Fluid Mech.* **258**, 77–104.

Hallworth, M. A., Hogg, A. J. & Huppert, H. E. 1998 Effects of external flow on compositional and particle gravity currents. *J. Fluid Mech.* **359**, 109–142.

Harris, T. C., Hogg, A. J. & Huppert, H. E. 2001 A mathematical framework for the analysis of particle-driven gravity currents. *Proc. R. Soc. Lond.* A **457**, 1241–1272.

Hatcher, L., Hogg, A. J. & Woods, A. W. 2000 The effects of drag on turbulent gravity currents. *J. Fluid Mech.* **416**, 297–314.

Hogg, A. J. & Huppert, H. E. 2001 Spreading and deposition of particulate matter in uniform flow. *J. Hydr. Res.* **39**, 505–518.

Hogg, A. J. & Pritchard, D. 2004 The effects of drag on dam-break and other shallow inertial flows. *J. Fluid Mech.* **501**, 179–212.

Hogg, A. J., Ungarish, M. & Huppert, H. E. 2000 Particle-driven gravity currents: asymptotic and box-model solutions. *Eur. J. Mech.* **338**, 139–165.

Hogg, A. J. & Woods, A. W. 2001 The transition from inertia to botton-drag-dominated motion of turbulent gravity currents. *J. Fluid Mech.* **449**, 201–224.

Hopfinger, E. J. 1983 Snow avalanche motion and related phenomena. *Annu. Rev. Fluid Mech.* **15**, 47–76.

Hoult, D. P. 1972 Oil spreading on the sea. *Annu. Rev. Fluid Mech.* **2**, 341–368.

Huppert, H. E. & Simpson, J. E. 1980 The slumping of gravity currents. *J. Fluid Mech.* **99**, 785–799.

Iverson, R. M. 1997 The physics of debris flows. *Rev. Geophys.* **35**, 245–296.

Klemp, J. B., Rotunno, R. & Skamarock, W. C. 1994 On the dynamics of gravity currents in a channel. *J. Fluid Mech.* **269**, 169–198.

Kneller, B. C., Bennett, S. J. & McCaffrey, W. D. 1999 Velocity structure, turbulence and fluid stresses in experimental gravity currents. *J. Geophys. Res.* **104**, 5381–5391.

Lane-Serff, G. F. 1993 On drag limited gravity currents. *Deep Sea Res.* **40**, 1699–1702.

Lewis, R. 1997 *Dispersion in Estuaries and Coastal Waters.* Wiley.

Linden, P. F. & Simpson, J. E. 1990 Continuous two-dimensional releases from an elevated source. *J. Loss Prev. Process Ind.* **3**, 82–87.

Linden, P. F. & Simpson, J. E. 1994 Continuous releases of dense fluid from an elevated point source in a cross-flow. In *Mixing and Transport in the Environment* (ed. K. J. Bevan, P. C. Chatwin & J. H. Millbank), Vol. 317, pp. 401–418. J. Wiley and Sons Ltd.

Martin, D. & Nokes, R. 1988 Crystal settling in vigorously convecting magma chamber. *Nature* **332**, 534–536.

Morton, B. R., Taylor, G. I. & Turner, J. S. 1956 Turbulent gravitational convection from maintained and instantaneous sources. *Proc. R. Soc. Lond.* A **234**, 1–23.

Parker, G. 1976 On the cause and characteristic scales of meandering and braiding in rivers. *J. Fluid Mech.* **76**, 457–480.

Peregrine, D. H. 1972 Equations for water waves and the approximations behind them. In *Waves on Beaches and Resulting Sediment Transport* (ed. R. Meyer), Chap. 3, pp. 95–121. Academic.

Ross, A. N., Tompkins, A. M. & Parker, D. J. 2004 Simple models of the role of surface fluxes in convective cold pool evolution. *J. Atmos. Sci.* **61**, 1582–1595.

Rottman, J. W., Hunt, J. C. R. & Mercer, A. 1985 The initial and gravity-spreading phases of heavy-gas dispersion: comparison of models with phase i data. *J. Hazard. Mat.* **11**, 261–279.

Rottman, J. W. & Simpson, J. E. 1983 Gravity currents produced by instantaneous releases of heavy fluid in a rectangular channel. *J. Fluid Mech.* **135**, 95–110.

Schijf, J. B. & Schönfeld, J. C. 1953 Theoretical considerations on the motion of salt and freash water. In *Proc. Minn. Intl Hydraulics Conv.*, pp. 321–333.

Simpson, J. E. 1997 *Gravity Currents in the Environment and the Laboratory*. Cambridge University Press.

Simpson, J. E. & Britter, R. E. 1979 The dynamics of the head of a gravity current advancing over a horizontal surface. *J. Fluid Mech.* **94**, 477–495.

Simpson, J. E. & Britter, R. E. 1980 A laboratory model of an atmospheric mesofront. *Q. J. R. Met. Soc* **106**, 485–500.

Sorgard, E. 1991 A numerical, three-layered, stationary salt wedge model. *J. Geophys. Res.* **96**, 12739–12754.

Turner, J. S. 1973 *Buoyancy Effects in Fluids.* Cambridge University Press.

Ungarish, M. & Huppert, H. E. 1998 The effects of rotation on axisymmetric particle-driven gravity currents. *J. Fluid Mech.* **362**, 17–51.

Whitham, G. B. 1974 *Linear and Nonlinear Waves.* Wiley.

Zhu, D. Z. & Lawrence, G. A. 2000 Hydraulics of exchnage flows. *J. Hydr. Engng* **126**, 921–928.